

PHYSICAL PROPERTIES OF CdSe THIN FILMS PRODUCED BY THERMAL
EVAPORATION AND E-BEAM TECHNIQUES

A THESIS SUBMITTED TO
THE GRADUATE SCHOOL OF NATURAL AND APPLIED SCIENCES
OF
MIDDLE EAST TECHNICAL UNIVERSITY

BY

ŞABAN MUSTAFA HUŞ

IN THE PARTIAL FULFILMENT OF THE REQUIREMENTS
FOR
THE DEGREE OF MASTER OF SCIENCE
IN
PHYSICS

SEPTEMBER 2006

Approval of the Graduate School of Natural and Applied Sciences

Prof. Dr. Canan Özgen
Director

I certify that this thesis satisfies all the requirements as a thesis for the degree of Master of Science.

Prof. Dr. Sinan Bilikmen
Head of Department

This is to certify that we have read this thesis and that in our opinion it is fully adequate, in scope and quality, as a thesis for the degree of Master of Science.

Prof. Dr. Mehmet Parlak
Supervisor

Examining Committee Members

Prof. Dr. Çiğdem Erçelebi	(METU,PHYS)	_____
Prof. Dr. Mehmet Parlak	(METU,PHYS)	_____
Prof. Dr. Bülent Akınoğlu	(METU,PHYS)	_____
Prof. Dr. Raşit Turan	(METU,PHYS)	_____
Prof. Dr. Bahtiyar Salamov	(Gazi Univ., PHYS)	_____

I hereby declare that all information in this document has been obtained and presented in accordance with academic rules and ethical conduct. I also declare that, as required by these rules and conduct, I have fully cited and referenced all material and results that are not original to this work.

Name, Last name : Şaban Mustafa HUŞ

Signature :

ABSTRACT

PHYSICAL PROPERTIES OF CdSe THIN FILMS PRODUCED BY THERMAL EVAPORATION AND E-BEAM TECHNIQUES

Huş, Şaban Mustafa

M.Sc., Department of Physics

Supervisor: Prof. Dr. Mehmet Parlak

September 2006, 84 pages

CdSe thin films were deposited by thermal evaporation and e-beam evaporation techniques on to well cleaned glass substrates. Low dose of boron have been implanted on a group of samples. EDAX and X-ray patterns revealed that almost stoichiometric polycrystalline films have been deposited in (002) preferred orientation. An analysis of optical measurements revealed a sharp increase in absorption coefficient below 700 nm and existence of a direct allowed transition. The calculated band gap was around 1.7 eV. The room temperature conductivity values of the samples were found to be between 9.4 and $7.5 \times 10^{-4} (\Omega\text{-cm})^{-1}$ and 1.6×10^{-6} and $5.7 \times 10^{-7} (\Omega\text{-cm})^{-1}$ for the thermally evaporated and e-beam evaporated samples respectively. After B implantation conductivity of these films increased 5 and 8 times respectively. Hall mobility measurements could be performed only on the thermally evaporated and B-implanted e-beam evaporated samples and found to be between 8.8 and $86.8 (\text{cm}^2/\text{V.s})$. The dominant conduction mechanism were determined to be thermionic emission above 250 K for all samples. Tunneling and

variable range hopping mechanisms have been observed between 150-240 K and 80-140 K respectively. Photoconductivity – illumination intensity plots indicated two recombination centers dominating at the low and high regions of studied temperature range of 80-400 K. Photoresponse measurements have corrected optical band gap measurements by giving peak value at 1.72 eV.

Keywords: CdSe, Thin film, Thermal evaporation, E-beam evaporation, Optical energy gap, Conductivity, Photoconductivity, Photoresponse.

ÖZ

TERMAL BUHARLAŞTIRMA VE E-DEMETİ TEKNİKLERİ KULLANILARAK ÜRETİLMİŞ CdSe İNCE FİMLERİN FİZİKSEL ÖZELLİKLERİ

Huş, Şaban Mustafa

Yüksek Lisans, Fizik Bölümü

Tez Yöneticisi: Prof. Dr. Mehmet Parlak

Eylül 2006, 84 sayfa

CdSe ince filimler ısısal buharlaştırma ve elektron demeti buharlaştırma teknikleri ile iyi temizlenmiş cam tabanlar üzerine büyütülmüştür. Örneklerin bir kısmı üzerine düşük dozda bor ekilmiştir. EDAX ve X-ışını analizleri hemen hemen bire bir oranlı çoklu kristal filimlerin (002) tercihli yönünde büyüdüğünü göstermiştir. Optik ölçümlerin analizi yaklaşık 700 nm dalga boyunda soğurmanın hızlı bir şekilde arttığını ve doğrudan izin verilmiş bir geçiş olduğunu göstermiştir. Filimlerin yasak enerji aralığının 1.7 eV civarında olduğu tespit edilmiştir. Isısal buharlaştırma ve elektron demeti ile buharlaştırma teknikleri ile büyütülmüş örneklerin oda sıcaklığındaki iletkenlik değerlerinin sırasıyla 9.4 ile $7.5 \times 10^{-4} (\Omega\text{-cm})^{-1}$ ve 1.6×10^{-6} ile $5.7 \times 10^{-7} (\Omega\text{-cm})^{-1}$ arasında değiştiği gözlemlenmiştir. Bor ekimi sonrasında bu filimlerin iletkenliklerinin sırasıyla 5 ve 8 kat arttığı gözlenmiştir. Mobilite ölçümleri sadece ısısal buharlaştırma ile hazırlanmış veya elektron demeti ile buharlaştırma tekniği ile hazırlanıp bor ekilmiş örnekler üzerinde yapılabilmektedir ve 8.8 ile 86.8 ($\text{cm}^2/\text{V.s}$) arasında değişen mobilite değerleri bulunmuştur. Bütün

örneklerde ısısal saçılmanın 250 K üzeri sıcaklıklarda baskın iletim mekanizması olduğu, 150-240 K ve 80-140 K sıcaklık aralıklarında sırasıyla tünelleme ve değişken erimli hoplama mekanizmaları olduğu gözlenmiştir. Aydınlanma şiddeti-fotoakım grafikleri, ölçümlerin yapıldığı sıcaklık aralığı olan 80-400 K aralığının alt ve üst bölgelerinde baskın olan iki tekrar bileşim merkezinin varlığını ortaya koymuştur. Fototepki ölçümleri 1.72 eV tepe değeri vererek optik geçirgenlik ölçümlerini doğrulamıştır.

Anahtar Kelimeler: CdSe, İnce filim, Isısal buharlaştırma, elektron demeti ile buharlaştırma, İletkenlik, Optik enerji aralığı, Fotoakım, Fototepki.

To My Lovely Family

ACKNOWLEDGMENTS

I would like to express my deep gratitude and thanks to my supervisor Prof. Dr. Mehmet Parlak for his excellent supervision, valuable support and encouragement throughout this work. It was a great honor and privilege for me to work with his supervision and to share his valuable knowledge and expertise.

I would also like to present my sincere thanks to my dear lab colleagues Tahir Çolakođlu, Murat Kaleli and Mustafa Kulakçı for their kind friendship, help and useful cooperation.

My special thanks go to my dear roommates Sevi İnce and Elif Yurdanur and my dear friends İsmail Çıfci, İnanç Kanık, Beste Korutlu and Burhan Kıracı for their continuous encouragement, fruitful discussions, relaxing advices and endless patience.

With a deep sense of gratitude, I wish to express my thanks to my family for their understanding, encouragement, trust and for the support they provided me through my entire life.

Finally I would like to express my deepest thanks to Gül Esra Bülbul for her endless patience, understanding and valuable support I needed in order to complete this study.

TABLE OF CONTENTS

ABSTRACT	iv
ÖZ.....	vi
ACKNOWLEDGMENTS.....	ix
TABLE OF CONTENTS	x
LIST OF TABLES	xii
LIST OF FIGURES.....	xiii
CHAPTERS	
1. INTRODUCTION.....	1
2. THEORETICAL CONSIDERATIONS.....	3
2.1 Introduction.....	3
2.2 Material Properties.....	3
2.2.1 Structural, Electrical and Optical Properties of CdSe Single Crystals.....	3
2.2.2 Properties of Polycrystalline Thin Films.....	5
2.3 Conduction Mechanisms in Polycrystalline Thin Films.....	6
2.3.1 Thermionic Emission.....	7
2.3.2 Tunneling.....	10
2.3.3 Hopping.....	12
2.3.4 Hall Effect.....	15
2.4 Photoconductivity.....	17
2.4.1 Intrinsic Photoexcitation.....	18
2.4.2 One center recombination model.....	18
2.4.3 Two center recombination model.....	20
2.5 Optical Properties of Polycrystalline thin films.....	21
3. EXPERIMENTAL TECHNIQUES.....	24
3.1 Introduction.....	24
3.2 The Preparation of CdSe Thin films.....	24

3.2.1	Substrate and Sample Preparation.....	24
3.2.2	Growth Process of CdSe Thin Films.....	26
3.2.3	Annealing	30
3.2.4	Electrical Contacts	30
3.3	Structural Characterization	31
3.4	Electrical Measurements	32
3.4.1	Resistivity Measurements	32
3.4.2	Hall Effect Measurements.....	36
3.5	Photoconductivity	39
3.6	Optical Measurements	42
4.	RESULTS AND DISCUSSION.....	43
4.1	Introduction.....	43
4.2	Structural and Compositional Characterization	43
4.2.1	EDXA Results.....	44
4.2.2	XRD Measurements	45
4.3	Optical Characterization	52
4.4	Electrical Characterization.....	57
4.4.1	Conductivity Measurements and Conduction Mechanisms.....	57
4.4.2	Determination of Carrier Concentration and Mobility.....	66
4.5	Photoconductivity Analysis	68
5.	CONCLUSIONS	77
	REFERENCES	81

LIST OF TABLES

TABLES

Table 2-1: Crystal parameters (a, b, c) for different CdSe phases.	4
Table 3-1: Measured voltages for Van der Pauw method.	34
Table 3-2: Voltage measurements for Hall-bar samples.	37
Table 3-3: Hall -voltage measurements for Van der Pauw samples.	38
Table 3-4: Illumination intensity of the halogen lamp for given current values.	39
Table 4-1: Summary of deposition parameters of samples.	44
Table 4-2: Positions, properties and measured relative intensities of asgrown CdSe thin films.	48
Table 4-3: Summary of deposition conditions and main peak intensities.	48
Table 4-4: Optical band gap energies of asgrown samples.	54
Table 4-5: Summary of the conductivity, mobility and carrier density values of as grown samples at room temperature.	58
Table 4-6: The activation energy (E_a) of as grown CdSe thin films obtained from the temperature dependent conductivity measurements.	61

LIST OF FIGURES

FIGURES

Figure 2-1: Wurtzite (left) and sphalerite (right) structures referred to hexagonal axes.....	5
Figure 2-2: Energy band diagram of n type polycrystalline semiconductor in an external field.....	7
Figure 2-3: Energy Band Diagram for heavily doped polycrystalline thin film.....	11
Figure 2-4: a) Occupied and empty localized states between conduction and valance bands. b) Excitation of the carrier to the conduction band. c) Hopping conduction.....	12
Figure 2-5: Schematic Diagram of Hall effect.....	16
Figure 2-6: Energy band diagram for the intrinsic photoexcitation.....	19
Figure 2-7: Energy band structure for one center recombination model.....	20
Figure 2-8: Energy band diagram for a two center recombination model.....	20
Figure 2-9: Direct (a) and indirect (b) transitions.....	22
Figure 3-1: Van der Pauw (Maltase-Cross) geometry, and Hall bar (Six-arm bridge) geometry.....	25
Figure 3-2: Van der Pauw and Hall bar metal contact geometry.....	26
Figure 3-3: Illustration of the thermal evaporation system utilized in the deposition of CdSe thin films.....	28
Figure 3-4: The hot plate setup for annealing process.....	29
Figure 3-5: Illustration of the metallic evaporation system.....	31
Figure 3-6: Illustration of the liquid nitrogen, sample-in-vacuum type cryostat.....	33
Figure 3-7: Experimental arrangement for resistivity measurements a) Hall-bar samples b) Van der Pauw samples.....	35
Figure 3-8: Experimental arrangement for Hall effect measurements for van der Pauw geometry.....	38

Figure 3-9: Experimental setup for the measurements of photoconductivity.	40
Figure 3-10: Experimental setup for wavelength dependent photoconductivity measurements.	41
Figure 3-11: The illumination intensity wavelength dependence of the halogen lamp used in the wavelength dependent photoconductivity measurements.	42
Figure 4-1: EDXA patterns for T3 samples a) Asgrown, b) Annealed at 400°C in N ₂ atmosphere, c) Annealed at 250° under rough vacuum, d) Annealed at 500° under rough vacuum.	46
Figure 4-2: XRD diffractograms of the as grown CdSe thin films deposited at different evaporation cycles.	47
Figure 4-3: X-ray diffraction patterns of samples a) T1, b) T2, c) T3, d) E3 for different annealing levels.	50
Figure 4-4: Typical Transmission spectra (Sample T3 AsGrown)	52
Figure 4-5: Comparison of $(\alpha h\nu)^2$ and $(\alpha h\nu)^{1/2}$ plots.	54
Figure 4-6: The variation of $(\alpha h\nu)^2$ as a function of $h\nu$ for all as grown samples.	55
Figure 4-7: The variation of $(\alpha h\nu)^2$ as a function of $h\nu$ for selected samples. a) T2, b) T3, c) E3	56
Figure 4-8: The variation of $(\alpha h\nu)^2$ as a function of $h\nu$ for as grown, as implanted and annealed samples a) T2, b) E3.	56
Figure 4-9: Typical I-V characteristics for CdSe thin Films with indium contacts.	58
Figure 4-10: Temperature dependent conductivity of thermally evaporated (left axis) and e-beam evaporated (right axis) as grown CdSe thin films.	59
Figure 4-11: The variation of $\ln(\sigma T^{1/2})$ as a function of the inverse absolute temperature for a) thermally evaporated, b) e-beam evaporated CdSe samples.	62
Figure 4-12: Variation of conductivity as a function of temperature for unimplanted and B implanted CdSe thin films.	63

Figure 4-13: The variation of $\ln(\sigma T^{1/2})$ as a function of the inverse absolute temperature for a) unimplanted T2, b) B implanted T2 CdSe samples at various annealing temperatures.	63
Figure 4-14: The variation of $\ln(\sigma T^{1/2})$ as a function of the inverse absolute temperature for T3 samples.	64
Figure 4-15: a) $\ln(\sigma T^{1/2}) - T^{-1/4}$, b) $\sigma - T^2$, and c) $\ln(\sigma T^{1/2}) - 1000/T$ plots for as grown T3 samples.	65
Figure 4-16: The variation of $\ln(\mu T^{1/2})$ as a function of the inverse absolute temperature for B-implanted T2 samples.	67
Figure 4-17: Variation of conductivity as a function of inverse absolute temperature for as grown a) T4 and b) E1 samples.	69
Figure 4-18: The variation of photoconductivity as a function of inverse temperature at different light intensities for as grown a) T2 and b) E1 samples.	70
Figure 4-19: Photocurrent- illumination intensity behaviour at different temperatures for asgrown a) T2 and b) E1 samples.	72
Figure 4-20: Photocurrent- illumination intensity behavior at different applied electric fields for as grown a) T2 and b) E1 samples.	72
Figure 4-21: Photocurrent as a function of incident photon energy at different temperatures for as grown a) T2, b) B-imp T2 and c) B-imp E3 CdSe thin films.	74
Figure 4-22: Photocurrent as a function of incident photon energy at 300°K for a) T2, b) B-imp T2 CdSe thin film after various annealing steps.	75
Figure 4-23: The variation of photoconductivity as a function of inverse temperature at different light intensities for as grown Boron impT2 samples.	76

CHAPTER 1

INTRODUCTION

In recent years, there has been a rapid development in the field of II-VI group (CdSe, CdS, ZnSe, CdTe) semiconductor thin films owing to their wide range of applications. As an important member of this group of binary compounds cadmium selenide (CdSe) is of interest for its applications as high efficiency thin film transistors [1,2], solar cells [3,4], photoconductors [5], gas sensors [6,7], acousto optical devices [8], photographic photoreceptors [9]. Major attention has been given in recent years to investigate the electrical and optical properties of CdSe thin films in order to improve the performance of the devices and also for finding new applications [10-14].

Polycrystalline semiconductor materials have come under increased scrutiny because of their potential use in cost reduction for device applications. A variety of methods have been used to prepare CdSe thin films including physical vapour deposition, sputtering spray pyrolysis, electrode deposition, molecular beam epitaxy, laser ablation and chemical deposition methods [15-24]. The physical vapour deposition and its variants are often used because they offers many possibilities to modify the deposition parameters and to obtain film with determined structures and properties [25].

Depending upon preparation conditions, CdSe single crystals crystallizes either as sphalerite (cubic, zinc blende) structure with space group $F\bar{4}3m$ or as wurtzite (hexagonal, zinc selenide) structure with space group P_3mc [26-28]. Similar dimorph structure is observed for the CdSe thin films. Although most of the researchers have reported hexagonal structure with the c axis oriented normal to the substrate surface [25, 29, 30] there are several studies [31] indicating the cubic structure for the CdSe polycrystalline thin films.

CdSe thin films with absorption edge at about 700 nm have a direct band gap of 1.7 eV at room temperature which makes them a good candidate for solar cells, light emitting diodes, photo-detectors and other opto-electronic devices. CdSe is widely preferred in fabrication of these devices owing to its high photosensitive behavior compared to the other II-VI materials [32].

The conduction mechanism in compound thin films is mainly governed by the grain boundary defect states [33]. In pure compound films like CdSe, the grain boundary core contains a large number of defects due to dangling bonds [34]. The native defects of CdSe are excess Cd and Se vacancies [10, 35, 36]. As a result of these defects CdSe often possesses n-type conductivity in bulk as well as in thin films if it is not doped intentionally. Those defects effectively act as either trapping or recombination centers and play an important role in the conduction processes in CdSe thin films [34]. Concentration of native defects is dependent on film growth conditions.

In this study, we have tried to get the electrical, structural and optical properties and distinctions of CdSe thin films grown by thermal evaporation and e-beam evaporation techniques using CdSe powder by means of X-ray analysis, energy dispersive X-ray analysis (EDAX), temperature dependent mobility and conductivity measurements in the temperature range of 100-400 K, photocurrent-illumination intensity and spectral photocurrent dependencies. The effect of Boron doping was also studied by comparing the data obtained from unimplanted samples. Systematic annealing on the unimplanted and implanted samples was carried out to deduce the effect of post annealing on the electrical and physical properties of the films.

CHAPTER 2

THEORETICAL CONSIDERATIONS

2.1 Introduction

The structural, electrical and the optical properties of CdSe single crystals are given and general properties of polycrystalline semiconductors with a special emphasis on the CdSe thin films are introduced in the first section of this chapter. Starting from the second section theoretical basis of general conduction mechanisms, photoconductivity concept and optical absorption in polycrystalline semiconductor films has been discussed in a more detailed manner.

2.2 Material Properties

2.2.1 Structural, Electrical and Optical Properties of CdSe Single Crystals

The compound CdSe belongs to the family of semiconductors of the II-VI type. CdSe Like the other II-VI compounds is dimorph at ordinary pressures. Depending upon preparation conditions, CdSe single crystals crystallizes either as sphalerite (cubic, zinc blende) structure with space group $\overline{F43m}$ or as wurtzite (hexagonal, zinc selenide) structure with space group P_3mc [26–28]. Sphalerite is the stable low temperature phase and the cubic-to-hexagonal transition occurs at $T_C = (95 \pm 5) ^\circ C$ [37]. In parallel to this result Yeh et al. [38] have calculated a positive energy difference between hexagonal and cubic structures. However, the energy difference is only a few meV per atom so when the samples are prepared at temperatures higher than T_C the wurtzite structure is retained at room temperature.

Table 2.1 gives crystal parameters of cubic and hexagonal phases taken from the IDDC database Card No. 19-0191 and IDDC Card No. 08-0459 respectively.

Table 2-1: Crystal parameters (a, b, c) for different CdSe structures.

Crystal Structure	a (Å)	b (Å)	c (Å)
Cubic	6.077	6.077	6.077
Hexagonal	4.299	4.299	7.010

When both of the wurtzite and sphalerite structures are referred to hexagonal axes as in fig.2.1, it becomes clear that they are strictly related from a geometrical point of view [26-28]. In constructing the hexagonal cell of the sphalerite, the cubic [111] direction is taken as hexagonal [001], with hexagonal axes related to the cubic ones as $c_h = \sqrt{3}a_c$ and $a_h = (1/\sqrt{2})a_c$. As can be seen, the two forms differ essentially for the packing along the ternary axis, which is of the kind fcc (i.e., *ABC*) in the sphalerite and hcp (i.e., *AB*) in the wurtzite [39].

CdSe Single crystals have a specific density of 5.816 g/cm³ and melting point of 1541 K. Hardness of these crystals is about 4 MΩ and their thermal conductivity is 3.49 W m⁻¹ K⁻¹ [40].

CdSe single crystals exhibits n-type electrical conduction without doping intentionally and their conductivity ranges changes between 10⁻⁷-10¹ (Ω-cm)⁻¹. Hall mobility of CdSe single crystals has been measured to be between 325-1050 (cm²/V-s) [40,41]. CdSe single crystals with 2mm thickness transmit the light with wavelength between 0.53-15 μm. Their refraction index is 2.55 for incident light at 900 nm.

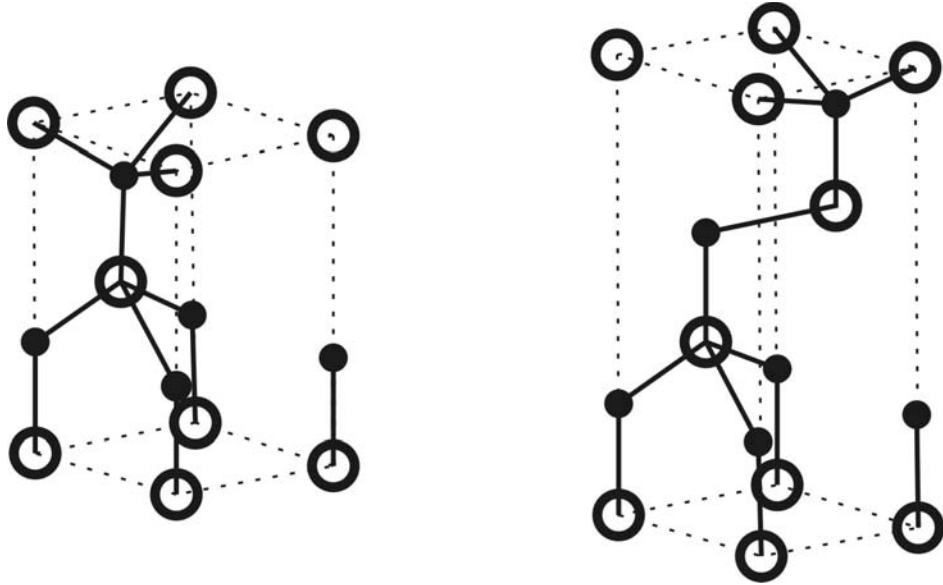


Figure 2-1: Wurtzite (left) and sphalerite (right) structures referred to hexagonal axes. Se atoms are represented by large white circles and Cd atoms by small black circles. The cubic [111] direction of sphalerite is taken as hexagonal [001]. Hexagonal axes are related to the cubic ones as $c_h = \sqrt{3}a_c$ and $a_h = (1/\sqrt{2})a_c$.

2.2.2 Properties of Polycrystalline Thin Films

A solid material is said to be a thin film when it is built up as a thin layer on a solid support, called substrate. Composition of individual atomic, molecular or ionic species can be controlled during deposition either by physical processes and/or electrochemical reactions. Many techniques have been developed for thin film deposition. Vacuum evaporation, sputtering, molecular beam epitaxy and chemical deposition are the mostly used methods to grow thin films.

The differences between the bulk materials and their thin film forms arise because of their small thickness, large surface-to-volume ratio and unique physical structure which is a direct consequence of the growth process. Optical interference, electronic tunneling through an insulating layer, high resistivity and low temperature coefficient of resistance are some of the phenomena arising as a result of small thickness. The high surface-to-volume ratio of thin films due to their small thickness and microstructure can influence a number of phenomena such as gas absorption,

diffusion and catalytic activity [42]. It is not simply the thickness which endows thin films with special and distinctive properties. The most important differences between the bulk materials and their thin film forms are the result of microstructures produced by progressive addition of basic building blocks one by one. Films prepared by direct application of a dispersion or paste of the material on a substrate are called thick films irrespective of their thickness. Thick films have different properties than thin films.

Modern thin film technology has evolved into a sophisticated set of techniques used to fabricate many products. Applications include very large scale integrated (VLSI) circuits, sensors and devices; optical films and devices; as well as protective and decorative coatings.

2.3 Conduction Mechanisms in Polycrystalline Thin Films

Conductivity values of the polycrystalline thin film may completely differ from the conductivity values of the single crystal of the same material. The distinctions between polycrystalline thin films and single crystals are related to structural and surface effects, reduced mobility of the carriers colliding with the boundary interruptions and change in the carrier density due to space charge regions at the intra-grain interfaces. So transport mechanisms in polycrystalline thin films are strongly dominated by boundaries of the grains rather than the grains themselves [43]

Similar to the single crystal semiconductors, polycrystalline semiconductors have valance and conduction bands. Space-charge regions between grains bend these bands and create potential barriers to current carriers. Fig. 2.2 gives the energy band representation of an *n*-type polycrystalline semiconductor in an external electric field.

In general, three types of conduction mechanisms provide the current conduction through polycrystalline thin films. Thermionic emission, tunneling and hopping mechanisms dominate the current conduction at highest to lowest temperature regions, respectively. Following sections presents the theoretical background for these mechanisms.

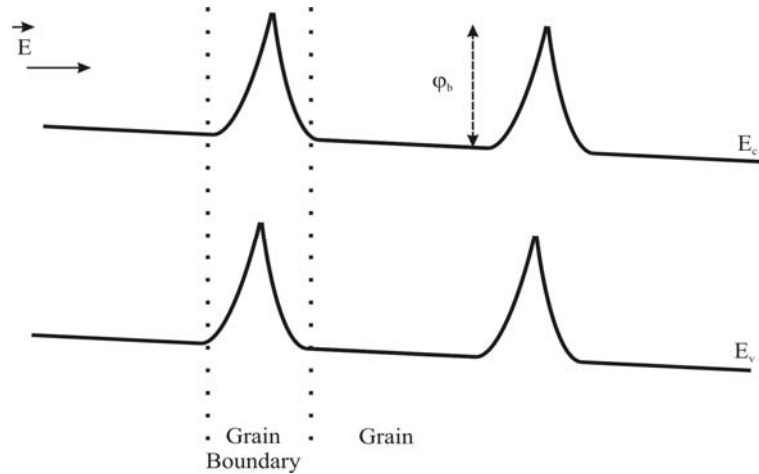


Figure 2-2: Energy band diagram of *n*-type polycrystalline semiconductor in an external field

2.3.1 Thermionic Emission

Various models have been proposed to explain the transport mechanisms analytically. The ones presented by Volger [44], Petritz [45], Berger [46,47] and Seto [48, 49] are general and pioneering models among them.

The first approach which was developed by Volger tried to explain the transport phenomena with ohmic conduction behavior of carriers in serially connected homogenous highly conductive grains and low conductive grain boundaries.

Petritz developed a better approach based on the thermionic emission of carriers from grain to grain. As Volger did, Petritz characterized the film with serially connected grain and grain boundary resistances but averaged them over many grains. A single grain and a single grain boundary with resistivities ρ_1 and ρ_2 respectively compose a region with total resistivity ρ_g

$$\rho_g = \rho_1 + \rho_2 \quad (2.3.1)$$

Petritz assumed that $\rho_2 \gg \rho_1$ and used diode equation for boundaries. After these assumptions current density- voltage (j - V) relation is written as

$$j = qn_a \left(\frac{kT}{2m^* \pi} \right)^{1/2} \exp\left(\frac{-q\phi_b}{kT}\right) \left[\exp\left(\frac{-qV_b}{kT}\right) - 1 \right] \quad (2.3.2)$$

where;

n_a : average majority carrier density in the grains,

ϕ_b : potential height of the barrier,

V_b : voltage drop across the barrier,

m^* : effective mass of the carriers.

Since a thin film is composed of many such cascaded regions, the voltage drop across a single unit is very small. So we can assume $V_b \ll kT/q$ and write equation 3.2.2 as,

$$j = q^2 n_a V_b \left(\frac{1}{2m^* \pi kT} \right)^{1/2} \exp\left(\frac{-q\phi_b}{kT}\right) \quad (2.3.3)$$

if there are n_c grains per unit length, conductivity can be written as

$$\sigma = q^2 \frac{n_a}{n_c} \left(\frac{1}{2m^* \pi kT} \right)^{1/2} \exp\left(\frac{-q\phi_b}{kT}\right) \quad (2.3.4)$$

Petriz observed that the exponential dependence of current density to $1/kT$ characterizes the barrier. His assumption $\rho_2 \gg \rho_1$ made him concluded that it is not the carrier concentration but the mobility has an exponential inverse temperature dependence; that is,

$$\mu_b = \mu_0 \exp\left(\frac{-q\phi_b}{kT}\right) \quad (2.3.5)$$

A more general form of Eq. 2.3.5 is obtained if scatterings within the grain are taken into consideration in this case $\mu_0 = \mu_b(T)$, the bulk value of mobility.

Berger extended Petriz model by demonstrating exponential relation of Hall coefficient and carrier concentration with $1/kT$. Berger showed that

$$R_H = R_0 \exp\left(\frac{E_n}{kT}\right) \quad (2.3.6)$$

so

$$n \propto \exp\left(\frac{-E_n}{kT}\right) \quad (2.3.7)$$

where E_n is the carrier activation energy which depends on the relative carrier concentration in grain and boundary regions. and will be discussed below. Contributions to the model are made by Mankarious [50] who observed that conductivity can be written in a more general form in terms of conductivity activation energy E_σ as

$$\sigma \propto \exp\left(-\frac{E_\sigma}{kT}\right) \quad (2.3.8)$$

since

$$\sigma = ne\mu_n \quad (2.3.9)$$

relationship between conductivity activation energy, carrier activation energy and barrier height can be predicted to be

$$E_\sigma \approx E_n + q\phi_b \quad (2.3.10)$$

Analogous to the Berger and Petritz models, grain boundary trapping model provided by Seto [48,49] is also based on potential barriers at grain boundaries. These barriers are produced by active trapping sites at the grain boundaries that capture free carriers and create space charge regions.

There are two possible conditions $Q_t > NL$ or $Q_t < NL$ where Q_t is trap density at the boundary surface (cm^{-2}), N is free carrier (impurity or doping) density (cm^{-3}) and L is the grain size.

If $Q_t > NL$ the grain is completely depleted from carriers and trap states are partially filled. Increase in the carrier concentration increases the strength of the dipole layer at boundaries so the barrier height. For this case average carrier concentration can be written as

$$n_a = \left(\frac{n_i}{qL}\right) \left(\frac{2\pi\epsilon kT}{N}\right)^{1/2} \exp\left(\frac{E_b + E_f}{kT}\right) \text{erf}\left[\frac{qL}{2} \left(\frac{N}{2\epsilon kT}\right)^{1/2}\right] \quad (2.3.11)$$

where n_i is the intrinsic carrier concentration of the single grain and

$$E_b = q\phi_b = \frac{q^2 l^2 N}{8\epsilon} \quad (2.3.12)$$

For the second case ($Q_t < NL$) only a partition of grain is depleted from carriers. Since all the traps are filled when $Q_t = NL$ further increase in the carrier concentration decreases the width of the dipole layer and barrier height. In this case,

$$n_a = n_i \exp\left[\frac{-(E_{vo} - E_f)}{kT}\right] \left[\left(1 - \frac{Q_t}{LN}\right) + \frac{1}{qL} \left(\frac{2\pi\epsilon kT}{N}\right)^{1/2} \right] \operatorname{erf}\left[\frac{qQ_t}{2} (2\epsilon kTN)^{1/2}\right]$$

and then by inserting this equation into Eqn. 2.3.4 the conductivity can be written as

$$\sigma \propto \exp\left[-\left(\frac{1}{2}E_g - E_f\right)/kT\right] \quad \text{for } Q_t > NL \quad (2.3.14)$$

and

$$\sigma \propto T^{-1/2} \exp\left(\frac{-E_b}{kT}\right) \quad \text{for } Q_t < NL \quad (2.3.15)$$

For both of the cases the effective mobility is

$$\mu_{eff} = \left(\frac{q^2 L^2}{2\pi m^* kT}\right)^{1/2} \exp\left(\frac{-q\phi_b}{kT}\right) \quad (2.3.16)$$

2.3.2 Tunneling

Thermionic emission model discussed above explains the most of the electrical properties of polycrystalline semiconductors at high temperatures. However, it is not enough to explain the saturation tendency appearing at low temperatures. In order to make a complete explanation of temperature dependence of conductivity other transport mechanisms have to be taken into consideration.

Quantum mechanical tunneling of carriers through high but narrow potential barriers at grain boundaries is one of the mechanisms limiting the resistivity of polycrystalline thin films.

Garcia et al [51] have developed a model that explains tunneling currents through In-doped CdS grain boundaries for partially depleted grain case with the energy band diagram given in Fig.2. They found the energy barrier height to be

$$\phi_b = \frac{q^2 N_T^2}{8\epsilon N_D} + \frac{2E_F}{5} \quad (2.3.17)$$

where N_T is the trap density and N_D is the carrier density.

Transmission probability of a carrier with energy E relevant to this potential barrier can be given in terms of WKB approximation as;

$$T = \exp\left(-2 \int \sqrt{\frac{2m^*(V-E)}{\hbar^2}} dx\right) \quad (2.3.18)$$

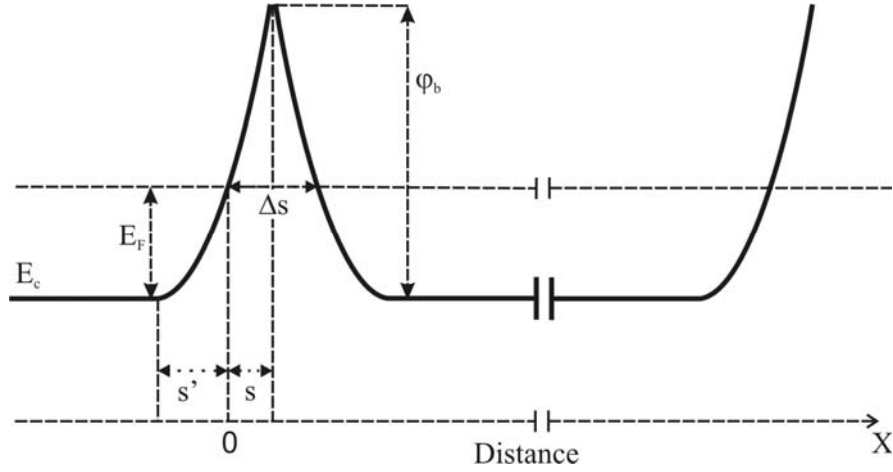


Figure 2-3: Energy band diagram for heavily doped polycrystalline thin film.

If a potential difference ΔV occurs at the barrier, the symmetry of the potential is lost. A suitable expression of the tunneling current density J_t was calculated by Simmons [52]. The net current which is calculated as the difference between the current from left to right and right to left, is expressed as

$$J_t = J_0 \left(\frac{FT}{\sin(FT)} \right) \quad (2.3.19)$$

with,

$$F = \frac{2\pi^2 k \Delta s \sqrt{2m^*}}{h \sqrt{\bar{\phi}_b}} \quad (2.3.20)$$

Where Δs is the barrier width, $\bar{\phi}_b$ is the average barrier height, m^* is the effective mass and J_0 is tunneling current density at 0 K which can be expressed as

$$J_0 = V \frac{q^2 \sqrt{2m^* \bar{\phi}_b}}{h^2 \Delta s} \exp \left(-\frac{4\pi \Delta s \sqrt{2m^* \bar{\phi}_b}}{h} \right) \quad (2.3.21)$$

If L is the grain size the film conductivity can be found using $\sigma_t = LJ_t/V$. For the small values of FT , σ_t can be expressed as

$$\sigma_t = \sigma_0 \left[1 + \left(\frac{F^2}{6} \right) T^2 \right] \quad (2.3.22)$$

2.3.3 Hopping

Energy band diagram of a semiconductor is not composed of only valance and conduction bands. Sufficient disorder in material can produce the characteristic solutions of the Schrödinger equation which are localized in space. Anderson [53] gave a quantitative criterion of localization for widely spaced and tightly bounded impurity states. Wave function of those states fall off exponentially with separation between states as $\exp(-\alpha R)$. Here α is the decay constant and R is the average distance between states.

In polycrystalline thin films, trap states at the grain boundaries act as localized states. Fig. 3.a shows energy band structure with such localized levels. Hopping of carriers between these states provides current through boundaries. At low temperatures, impurity concentrations for which thermionic emission and tunneling make small contributions to current density, hopping becomes the most dominant conduction mechanism. Mott and Davis [54] have given a successful model of this transport mechanism.

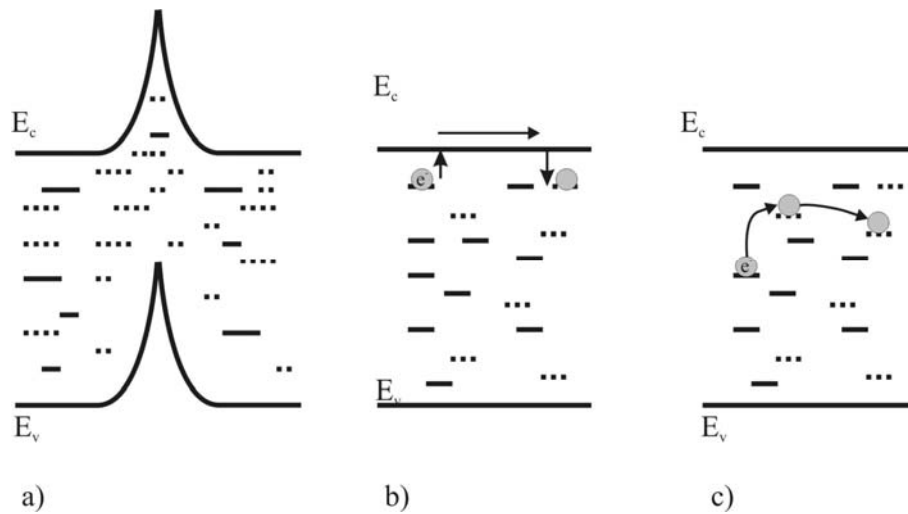


Figure 2-4: a) occupied (straight) and empty (dotted) localized states between conduction and valance bands. b) Excitation of the carrier to the conduction band. c) Hopping conduction.

if Fermi level is below the mobility edge, the conduction will be of two types:

i-)Excitation of the carriers to conduction band. The contribution of this process to the conductivity is

$$\sigma = \sigma_0 \exp\left(-\frac{E_c - E_f}{kT}\right) \quad (2.3.23)$$

This form of conduction is normally predominant at high temperatures or when $E_c - E_f$ is small. Figure 3.b illustrates this process.

ii-) Thermally activated transitions of carriers between localized states near the Fermi level. When an electron in an occupied state below E_f , receives energy from a phonon, it moves to a nearby state above E_f . Product of the following factors gives the probability per unit time that this event occurs.

- a) The Boltzmann factor ($\exp(-\Delta E/kT)$). Where ΔE is the energy difference between initial and final states.
- b) A factor v_{ph} depending on the phonon spectrum.
- c) A factor depending on the overlap of wave functions.

The last factor give rise to two types of hopping mechanism named according to the hopping range. First of them is constant range hopping, in which carriers can jump only to the nearest state, occurs only in the case of weak overlap i.e. $\alpha R \gg 1$. The second possibility is variable range hopping, in which carriers jump to another empty state away from the nearest one. This mechanism is always to be expected if αR is comparable with or less than unity, or in all cases at sufficiently low temperatures.

To find the conductivity for the constant range hopping, we must first write the difference of the hopping probabilities in two directions, such as;

$$\rho_{\pm} = v_{ph} \exp\left(-2\alpha R_0 - \frac{\Delta E \pm eR_0 F}{kT}\right) \quad (2.3.24)$$

where F is the applied field and $\Delta E \approx 1/R_0^3 N(E_f)$. To obtain the current density j we must multiply this factor by e , R and carrier density within an energy range of kT at the Fermi energy. So

$$j = eR(2kTN(E_f)) \left(v_{ph} \exp\left(-2\alpha R_0 - \frac{\Delta E}{kT}\right) \left(\sinh\left(\frac{eR_0 F}{kT}\right) \right) \right) \quad (2.3.25)$$

since $\sigma = j/F$ for weak fields conductivity can be written as

$$\sigma = 2e^2 R_0^2 N(E_f) \left(v_{ph} \exp\left(-2\alpha R_0 - \frac{\Delta E}{kT}\right) \right) \quad (2.3.26)$$

Mott [55] calculated the conductivity due to variable range hopping by pointing out that hopping distance increases with decreasing temperature. An electron can hop to a site within its hopping range R . There are $4\pi(R/R_0)^3 / 3$ such states with average hopping distance $3R/4$. Normally it will hop to site for which the activation energy is the minimum and equals to

$$\Delta E = \frac{3}{4\pi R^3 N(E_f)} \quad (2.3.27)$$

The most probable hopping distance can be calculated using average hopping distance and Eqn. 2.3.27

$$R_e = \left(\frac{3}{2\pi\alpha N(E_f)kT} \right)^{1/4} \quad (2.3.28)$$

Using Eqn.2.3.27 and 2.3.28 the hopping probability given in Eqn.2.3.24 reduces to

$$\rho = v_{ph} \exp\left(\frac{-B}{T^{1/4}}\right) \quad (2.3.29)$$

where

$$B = B_0 \left(\frac{\alpha^3}{kN(E_f)} \right)^{1/4} \quad (2.3.30)$$

with B_0 lying in the range 1.7 - 2.5. Furthermore the mean activation energy for variable range hopping is

$$\overline{\Delta E} = \frac{B}{3\pi R^3 N(E_f)} \quad (2.3.31)$$

Employing the same calculations used to obtain Eqn.25 the conductivity can be expressed as,

$$\sigma = \frac{\sigma_0}{\sqrt{T}} \exp\left[-\left(\frac{T_0}{T}\right)^{1/4}\right] \quad (2.3.32)$$

where

$$\sigma_0 = 3q^2 v_{ph} \left(\frac{N(E_f)}{8\pi\alpha k} \right)^{1/2} \quad (2.3.33)$$

$$T_0 = \frac{\lambda \alpha^3}{kN(E_f)} \quad (2.3.34)$$

in which λ is a dimensionless constant.

In polycrystalline materials the temperature range over which variable range hopping is predominant is related to the grain size. If $L \gg L_D$ variable range hopping has a small contribution to the conductivity even at very low temperatures. On the other hand if $L \ll L_D$ variable range hopping controls the conductivity over a considerable wide range of temperature. Where L_D is the Debye length which is given as

$$L_D = \left(\frac{\epsilon \epsilon_0 kT}{q^2 N} \right)^{1/2} \quad (2.3.35)$$

where ϵ is the dielectric constant and N is the impurity concentration of the material.

2.3.4 Hall Effect

An important measurement technique which is used to determine carrier concentration, carrier type, and the mobility of a semiconductor material, is the Hall effect method. Mobile charges are subject to Lorentz force when a magnetic field \vec{B} is introduced to a current carrying conductor. As a result of this force charges are accumulated to the edges of conductor and forms a dipole which is perpendicular to both \vec{B} and \vec{j} . Accumulation process continues until

$$\vec{B} \times \vec{v} = \vec{E} \quad (2.3.36)$$

where \vec{v} is the drift velocity of carriers, and \vec{E} is the electric field produced by accumulated carriers.

If $\vec{v} = \vec{v}_x$ and $\vec{B} = \vec{B}_z$ then $\vec{E} = -\vec{E}_y$. For the sample given in Fig. 2.5

$$I = t w n q v \quad (2.3.37)$$

Where n is the carrier (hole or electron) concentration. Using Eqn. 1 and 2, Hall voltage can be written as

$$V_H = \frac{B I}{t n q} \quad (2.3.38)$$

and the Hall coefficient is defined as

$$R_H = \frac{1}{nq} = \frac{tV_H}{BI} \quad (2.3.39)$$

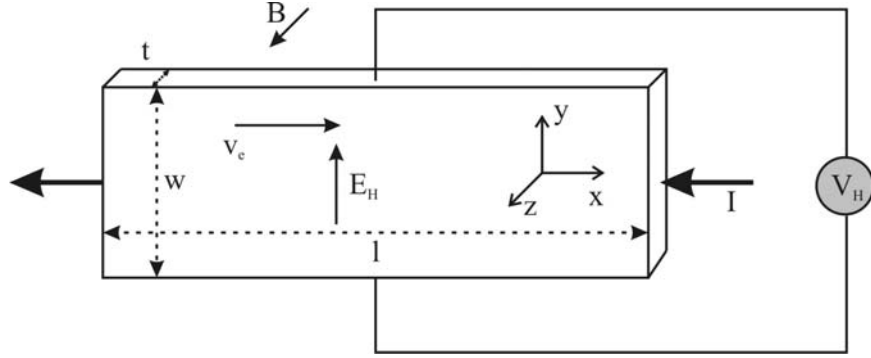


Figure 2-5: Schematic diagram of Hall effect.

Finally we can define the hall mobility using the relation $\sigma = nq\mu$, as

$$\mu_H = \sigma R_H \quad (2.3.40)$$

Measurement of the Hall voltage gives a direct measurement of carrier density and type. But Hall mobility does not give the complete definition of mobility in semiconductors. Actually there are four different types of mobility which must be differentiated from each other [56]. These mobility types are as follows;

i) The microscopic mobility is the mobility that free carriers actually have. This type of mobility can not be experimentally measured. If v_d is the drift velocity of the free carrier and E is the applied electric field microscopic mobility can be expressed as

$$\mu_{mic} = v_d / E \quad (2.3.41)$$

ii) “Conductivity mobility” is calculated from $\sigma = nq\mu$ and identical with the microscopic mobility for every practical purpose.

iii) Drift mobility is similar to the microscopic mobility but involves trapping processes.

iv) Hall mobility is the one obtained from Hall effect measurement.

2.4 Photoconductivity

Photoconductivity phenomena in a semiconductor material can be characterized with three basic quantities: the photosensitivity, the spectral response, and the speed of response [57]. Photosensitivity of a material is defined with the amount of photocurrent or with the ratio of photocurrent to the dark current. On the other hand, speed of response is how fast a material switches between steady state dark and photocurrent. Observation of transient process provides an important data to examine trap density. Dependence of photoconductivity to excitation wavelength is called as spectral response.

Since photoconductivity occurs as a result of photon absorption, a close correlation is expected between the optical absorption spectrum α vs. $h\nu$ and photoconductivity spectrum $\Delta\sigma$ vs $h\nu$. Photoconductivity is controlled by the surface lifetime in high absorption region while bulk lifetime is dominant in the low absorption region where the photons can penetrate into the material.

Both the carrier density and the carrier mobility of a semiconductor material may change under illumination. So dark conductivity of a semiconductor is given by Eqn.2.3.9 is increased by photoconductivity $\Delta\sigma$ as.

$$\sigma_0 + \Delta\sigma = q(n_0 + \Delta n)(\mu_0 + \Delta\mu) \quad (2.4.1)$$

Here only one type of carrier has been considered for simplicity. It is generally true that

$$\Delta n = G\tau_n \quad (2.4.2)$$

where G is the photoexcitation rate and τ_n is the free electron lifetime.

Several mechanisms may give rise to change in carrier mobility. Those mechanisms are:

- Density and cross section of charged impurities from which the carriers scatter may change under illumination.
- Photo excitation may decrease the height of the barriers and the width of depletion regions in polycrystalline materials.
- Carriers may be excited to a band with a different mobility.

Also an additional complexity arises from the fact that lifetime may be a function of excitation rate. If τ_n varies as $G^{\gamma-1}$, the $\Delta\sigma$ varies as G^γ . $\gamma > 1$ corresponds

to an increase in the lifetime with increasing excitation rate. This phenomena is called supralinear photoconductivity. Else if $\gamma < 1$ it is called sublinear photoconductivity.

Value of γ can be determined by measurement of the photoconductivity as a function of photoexcitation rate, and is used to specify appropriate model for the photoconductivity process. Three basic models causing different γ values will be discussed below.

2.4.1 Intrinsic Photoexcitation

The simplest model of photoexcitation assumes an energy-band diagram with no trap levels as shown in Fig 6. Photoexcitation rate G and thermal excitation rate g are balanced by the recombination across the band gap with a recombination rate R .

in dark

$$g = n_0 p_0 R = n_0^2 R \quad (2.4.3)$$

since $n_0 = p_0$ and $\Delta n = \Delta p$ for the intrinsic material, under illumination the above equation can be written as

$$G + g = (n_0 + \Delta n)R(p_0 + \Delta p) = (n_0 + \Delta n)^2 R \quad (2.4.4)$$

For the intrinsic material, it is usually true that $g \ll G$ and $n_0 \ll \Delta n$.

Therefore

$$G \propto (\Delta n)^2$$

since $\gamma = 0.5$ a case of sublinear photoconductivity is observed. Free carrier lifetime decreases with the increasing photoexcitation rate.

2.4.2 One center recombination model

Addition of a single trap level between valance and conduction bands radically changes the photoconductivity behavior. Fig. 7 shows the energy band diagram for this case. Only the transitions given in the figure are considered in this model. Thermal excitation is neglected and only one trap level with a density of N_t is included. Then, th generation rate at equilibrium can be written as

$$G = n\beta_n(N_t - n_t) \quad (2.4.5)$$

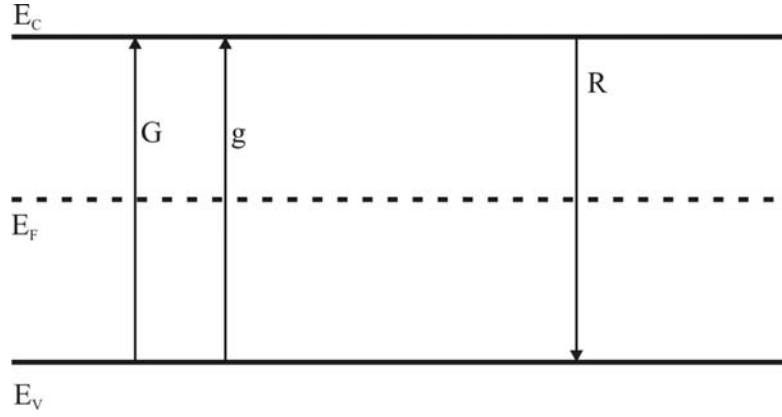


Figure 2-6: Energy band diagram for the intrinsic photoexcitation

$$n\beta_n(N_t - n_t) = n_i p \beta_p \quad (2.4.6)$$

$$G = n_i p \beta_p \quad (2.4.7)$$

where n_t is the density of occupied trap levels, β_n and β_p are electron and hole capture coefficients respectively. It is evident that only two of these equations are independent. However, one needs three equations for determination of generation rate, the missing equation comes from charge neutrality,

$$n = p + (N_t - n_t) \quad (2.4.8)$$

dependence of n and p on G can be determined from eqns.(2.4.5-2.4.8).

$$G = (N_t - G/n\beta_n)(n - G/n\beta_n)\beta_p \quad (2.4.9)$$

$$G = (N_t - G/p\beta_p)(p + N_t - G/p\beta_p)\beta_p \quad (2.4.10)$$

For small values of n or low intensity photoexcitation, there is a hole in the recombination center for every electron in the conduction band and almost all of the recombination centers are filled. So

$$n \approx (N_t - n_t) \approx 0$$

therefore, $G = n^2 \beta_n$ and $G = p N_t \beta_p$, the other limit case is large values of n or high intensity photoexcitation. If $\beta_p \gg \beta_n$ almost all of the recombination centers are empty and $n = p \propto G$

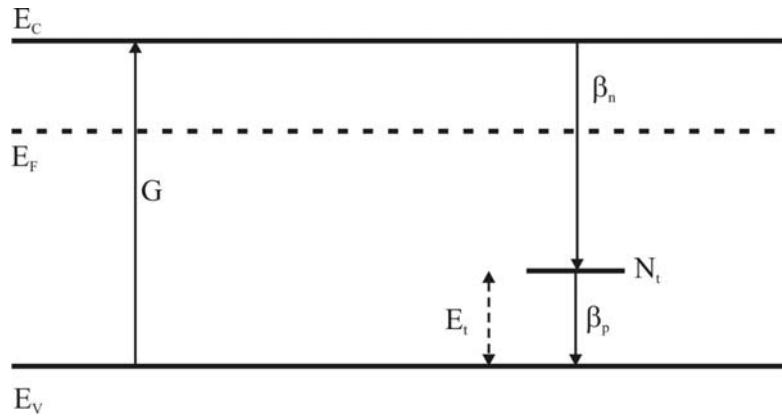


Figure 2-7 Energy band structure for one center recombination model.

2.4.3 Two center recombination model

Next step in the discussion of photoconductivity models is two center recombination model. Typical energy band diagram for an n type material with two trap levels is given in Fig.8. One of the trap levels in the figure is a sensitizing center which is a doubly negative acceptor with $\beta_p^S \approx \beta_p^R$ and $\beta_n^S \ll \beta_n^R$. Where the indexes S and R represent sensitizing centers and recombination centers respectively.

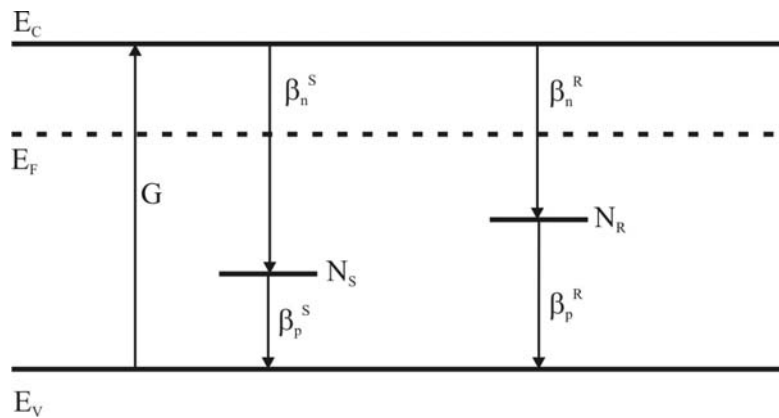


Figure 2-8: Energy band diagram for a two center recombination model.

As the addition of the first recombination center did above, the addition of the sensitizing center gives rise to new physical results. Some of them are

- Imperfection sensitization
- Supralinear photoconductivity
- Thermal quenching of photoconductivity
- Optical quenching of photoconductivity
- Negative photoconductivity
- Photoconductivity saturation

An abrupt decrease in photocurrent is observed when the temperature of the sample is raised above a critical value. The value of the critical temperature increases with increasing photoexcitation intensity. This is called thermal quenching and it is simply another way of looking supralinear photoconductivity phenomena [57] described above. If we plot $\Delta\sigma$ vs. G at constant temperature, we see supralinear photoconductivity, if we plot $\Delta\sigma$ vs. T at constant photoexcitation intensity, we see thermal quenching.

2.5 Optical Properties of Polycrystalline thin films

Investigation of optical properties of polycrystalline thin films generally focuses on optical band gap and refraction index calculations. A polycrystalline film is not solely composed of perfect bulk material separated by grain boundaries; it also includes defects like unwanted impurities, stoichiometry deviations, point defects. In general optical properties are less sensitive than electrical properties to those effects [58].

Optical band gap of a semiconductor material can be determined from the absorption spectrum of the material. A rapid rise in the absorption coefficient is observed when the incoming photons have enough energy to excite electrons from the valance band to the conduction band. Those band to band or exciton transitions are called fundamental absorption. However certain selection rules are effective on band to band transitions, so band gap can not be estimated in a straight forward manner, even if competing absorption process can be accounted for [59].

Basically two types of optical transition can occur at the fundamental edge of crystalline semiconductors, direct and indirect. Both of them involve photon electron interaction which is resulted with the excitation of the electron from valance band to the conduction band. If the electron has the same wave vector in both of bands the transition is said to be direct. But the electron may not have the same momentum in valance and conduction bands. In this case the electron must also have an interaction with phonons to transfer required momentum and the transition is said to be indirect.

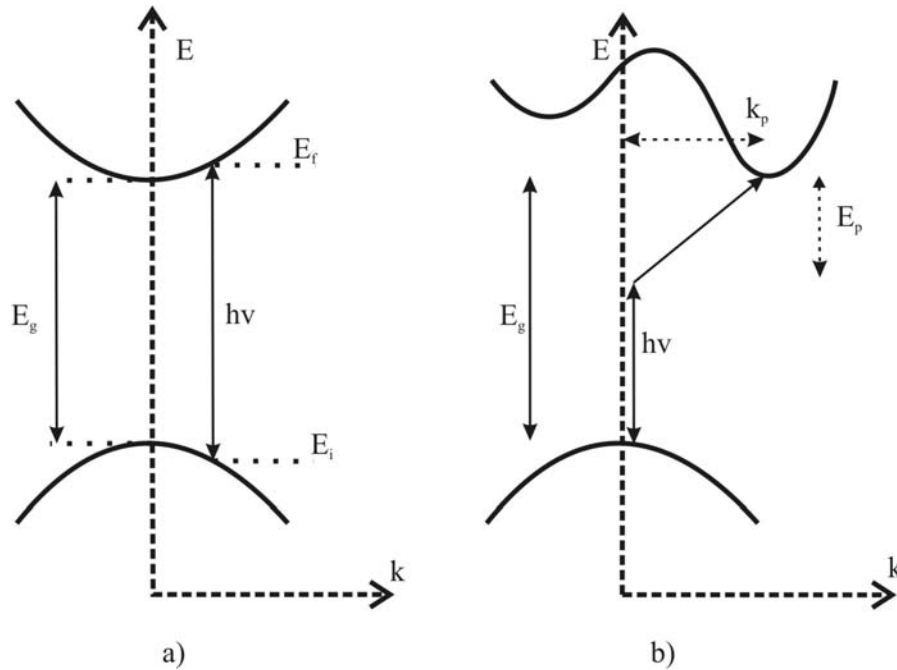


Figure 2-9: Direct (a) and indirect (b) transitions.

In a direct transition if all the momentum conserving transitions are allowed, the transition probability P_t is independent of photon energy and absorption coefficient has the following spectral dependence;

$$\alpha(h\nu) = A^*(h\nu - E_g)^{1/2} \quad (2.5.1)$$

where A^* is a function of reduced hole and electron masses. In some materials, quantum selection rules forbid direct transitions at $k = 0$ but allow them at $k \neq 0$.

Hence transition probability increases linearly with $(h\nu - E_g)$ and absorption coefficient is given as;

$$\alpha(h\nu) = A'(h\nu - E_g)^{3/2} \quad (2.5.2)$$

A two step process is required for an indirect transition because a change in both energy and momentum occurs. Since the photon has a very small momentum an interaction with a phonon is needed. Only the phonons which can supply the proper momentum change are usable. These are usually the longitudinal and transverse acoustic phonons. During the transition a phonon with characteristic energy E_p is either absorbed or emitted. Absorption coefficients for each case are,

$$\alpha_a(h\nu) = \frac{A(h\nu - E_g + E_p)^2}{\exp\left(\frac{E_p}{kT} - 1\right)} \quad \text{for } h\nu > E_g - E_p \quad (2.5.3)$$

and

$$\alpha_e(h\nu) = \frac{A(h\nu - E_g - E_p)^2}{1 - \exp\left(-\frac{E_p}{kT}\right)} \quad \text{for } h\nu > E_g + E_p \quad (2.5.4)$$

respectively. Since both of the processes are possible when $h\nu > E_g + E_p$ the absorption coefficient must be written as

$$\alpha(h\nu) = \alpha_a(h\nu) + \alpha_e(h\nu) \quad \text{for } h\nu > E_g + E_p \quad (2.5.5)$$

In addition to band to band absorption, impurity effects in the absorption spectrum may be observed. These effects include acceptor-conduction band, valance band-donor, and possibly acceptor-donor transitions, all on the low energy side of the absorption edge.

CHAPTER 3

EXPERIMENTAL TECHNIQUES

3.1 Introduction

In this chapter, the details of CdSe thin film growth and heat treatment procedure, structural, optical and electrical characterization methods and analysis of experimental data are summarized. The thin films were deposited on soda lime glass, tin oxide coated glass, indium thin oxide coated glass and silicon wafer substrates by the thermal evaporation and e-beam evaporation techniques. Hall-bar and van der Pauw mask geometries were used to examine electrical and electro-optical properties of the samples. Structural and compositional characterizations of the films were done by the help of X-ray diffraction (XRD) and the electron spectroscopy for chemical analysis (ESCA-XPS). Temperature dependent conductivity and Hall effect measurements in between 80-400 K are carried out to deduce the electrical characteristics of the films. Also temperature dependent photoconductivity measurements under different illumination intensities ranging from 17 to 113 mW/cm² and under different wavelength ranging between 350 and 950 nm have been carried out in the temperature range of 80-400 K. Optical transmission spectrum of films has been examined in the range of 200 to 1150 nm.

3.2 The Preparation of CdSe Thin films

3.2.1 Substrate and Sample Preparation

The soda lime glass, tin oxide coated glass, indium thin oxide coated glass, and silicon wafer substrates were used as substrate material for the deposition of CdSe thin films. The glass slides were prepared by cutting the commercial soda lime glass, into a suitable dimension compatible with the dimension of substrate holder by

using a diamond cutter tool. The glass slides were thoroughly cleaned before the deposition process in order for the glass substrates to attain a plausible sticking coefficient as the following procedure;

- The glass slides were first cleaned in a dilute solution of chemical detergent to remove the impurities and the protein materials on the surface of the slides.
- The same procedure of cleaning with detergent was repeated at a solution temperature of 70-100°C in a separate container.
- Rinsing with hot water was applied to remove the layer of detergent solution from the substrate surface.
- The glass slides were cleaned in a solution of trichloroethylene for 10 minutes and rinsed in hot water
- The glass slides were boiled in a solution of H₂O₂ 30% in order for the organic materials on the surface to gain the water solubility.
- Finally, the glass slides were rinsed in hot distilled water to get rid of the possible residues attained during the cleaning procedure.

The cleaning procedure was performed in an ultrasonic cleaner. The substrates, after the cleaning process, were kept in methanol. Prior to deposition the substrates were taken from the methanol and dried by blowing hot air or pure nitrogen.

The electrical measurements to be carried out acquire suitable sample geometries. The desired sample shapes used for the deposition of the films and metallization masks for these shapes are shown in Fig. 3.1 and 3.2, respectively.

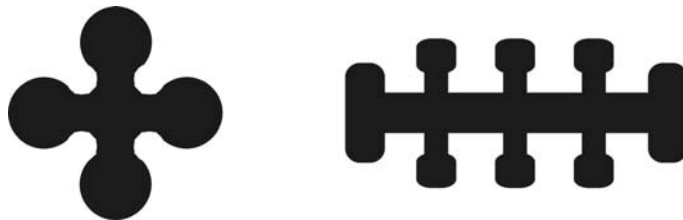


Figure 3-1: van der Pauw (Maltase-Cross) geometry, and Hall bar (Six-arm bridge) geometry.

The thin films are deposited in the six-arm-bridge (sometimes called as Hall-bar) and the “Maltese cross” geometry, which are appropriate for the standard Hall effect measurements and van der Pauw method respectively.

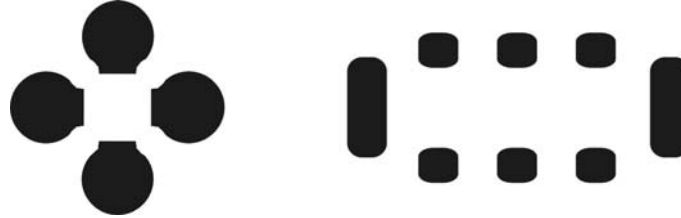


Figure 3-2: van der Pauw and Hall bar metal contact geometry.

3.2.2 Growth Process of CdSe Thin Films

The thermally evaporated grown CdSe thin films were all deposited in a Varian 3117 vacuum system. This system basically consists of a rotary vane mechanical pump, an oil diffusion pump with liquid nitrogen trap and a bell-jar vacuum chamber with gauges, deposition sources, substrate holder and other accessory equipment, as depicted in Fig. 3.3. Stainless steel bell-jar vacuum chamber is sealed to a stainless steel base plate with a rubber gasket. The base plate provides a large port for a pumping system and an array of smaller ports, or feedthroughs, for deposition sources and vacuum components. The lowest attainable pressure with this system is around 10^{-6} Torr. The fittings of the bell-jar were configured to be suitable for the growth of the thin films. A quartz ampoule, which is wound with molybdenum wire and situated within metal shields to stabilize the source temperature, was used to hold the source material and heat was produced by passing an electrical current through that wire. The temperature of the ampoule was manually controlled by manipulating the current supplied by the variac placed inside Varian 3117. The measurement of the temperature of the source was made by a Pt/Pt-13%Rh thermocouple, which is placed within the source and controlled by an Elimko-400 temperature controller.

A substrate heater was used to improve film adhesion, control grain structure and minimize the surface roughness. An aluminium block, which has holes along the length and chrome-nickel heating wires covered with insulating quartz tubes placed inside these holes, constitute the substrate heater. The substrates and the masks were placed in a sandwich structure between the aluminium holder containing nine rectangular holes suitable in size and aluminium substrate holder with heater. Copper sheets have been placed on the back side of the substrates to maintain a uniform substrate heating. The copper-constantan thermocouple was used to measure the temperature of the substrate, which had a place approximately 15 cm above the source. Again Elimko-400 temperature controller provided the control of the temperature at the substrate. A stainless steel shutter is mounted between the source and the substrate holder to start and stop the process of deposition.

The evaporation process can be organized to follow the procedure as follows; about 1 gr of CdSe were used as evaporation source material. The source material which was Alfa Aesar brand 99.995% pure CdSe, were powdered and placed in a quartz ampoule which was wound with a molybdenum-heating coil. The substrates were placed into the substrate holder together with the masks. After the vacuum pressure of about 5×10^{-6} Torr was reached, the source was heated up to 640 °C, which is the starting temperature for the evaporation of the CdSe, synchronously with the substrate. The temperature of the substrate was kept at a fixed value at 30, 150 and 200°C for different evaporation cycles. The shutter was opened to start the deposition process. The thickness and the growth rate of the films were measured by Inficon XTM/2 Deposition monitor. The deposition was stopped by closing the shutter when the required thickness was attained. The deposition rate was kept constant at 6 Å/sec through all of the growth cycles. In order to prevent possible oxidation of the films, system was allowed to cool down to room temperature after completing the deposition process, without disturbing the vacuum conditions.

A home made stainless steel vacuum chamber with Laybold turbo molecular pump were used for deposition of CdSe thin films with electron beam evaporation technique. At many points the growth process was similar with the thermal evaporation method discussed above. Again the vacuum chamber has been cleaned and the vacuum grease has been applied to rubber gasket before each run. The same

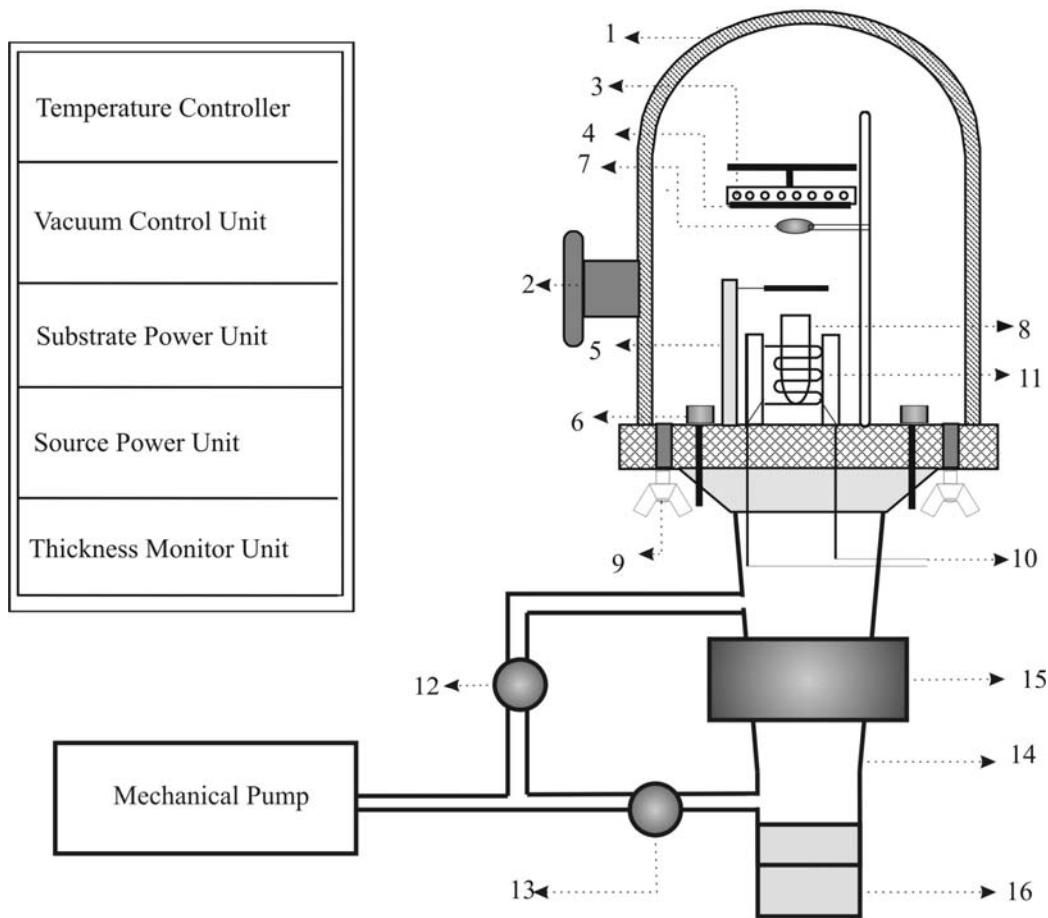


Figure 3-3: Illustration of the thermal evaporation system utilized in the deposition of CdSe thin films. 1. Stainless steel bell-jar, 2. Window, 3. Substrate heater, 4. Substrate holder, 5. Shutter, 6. Feedtrough, 7. Thickness monitor, 8. Source boat, 9. Air Valves, 10. Filament current wires, 11. Source heater 12. Roughing valve, 13. Foreline Valve, 14. Diffusion pump, 15. Liquid Nitrogen Trap, 16. Diffusion pump heater.

substrate holder, with substrates and masks in it, has been placed 15 cm above the evaporation source. The same kind and amount of source material within a 2 cm diameter graphite crucible has been placed in the water-cooled cavity of the electron beam source.

After the vacuum pressure of about 5×10^{-6} Torr was reached a 60 or 75 V_{rms} AC potential has been applied to substrate heater to obtain stable 150 or 200°C

substrate temperature respectively. Substrate temperature has been monitored by a Fluke digital thermometer with k-type thermocouple fastened on substrate holder. Power supply of e-beam source has been opened after all the substrates have reached the thermal equilibrium. Beam has been focused on the source by the help of the electromagnets and beam intensity has been adjusted to obtain desired evaporation and deposition rate. Then the shutter was opened to start the deposition process taking approximately 8 minutes. Deposition rate and film thickness has been measured by Inficon XTM/2 deposition monitor. The deposition rate has been kept about 6 Å/sec throughout the growth process. Shutter and e-beam source has been closed as soon as the desired thickness was reached. Monitored deposition rate dropped below 0.1 Å/s after this moment. After completing the deposition process, system was allowed to cool down to room temperature without disturbing the vacuum conditions. Following to the deposition of CdSe thin films, the thickness of the films were measured by Dektak 3030S profilometer.

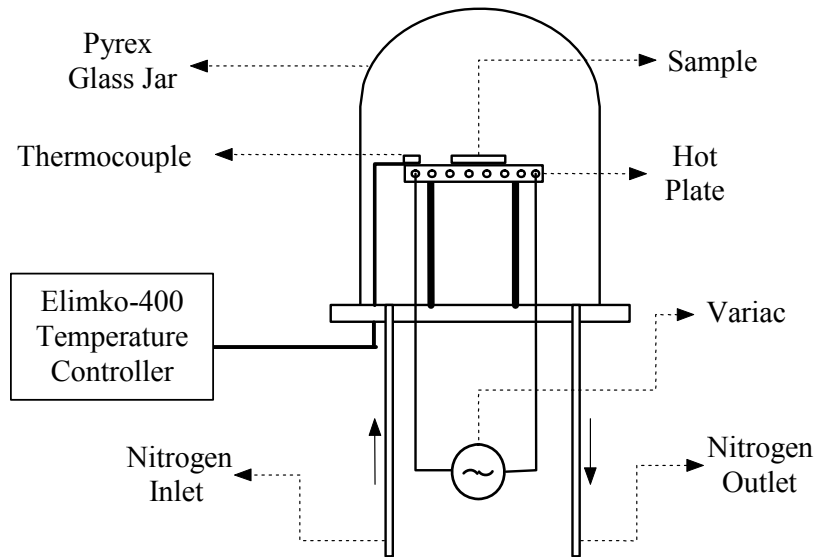


Figure 3-4: The hot plate setup for annealing process.

3.2.3 Annealing

Following the evaporation cycle, some of the CdSe films were annealed in nitrogen environment for 30 minutes at fixed temperatures in the range of 100-500 °C using the system pictured in Fig. 3.4. This system consists of chrome-nickel heating wires insulated by quartz tubes squeezed between two aluminium plates. The heating was supplied with a manually operated variac and the temperature on the plate was monitored with a NickelChrome-Nickel thermocouple and Elimko-400 Thermo-couple controller. During the heat treatment, continuous pure nitrogen gas flow was maintained.

3.2.4 Electrical Contacts

Indium contacts on CdSe thin films for electrical measurements were produced by metallic evaporation through the suitable contact masks onto samples. The metallic evaporations were performed by using Nanotech evaporator system as depicted in Fig. 3.5. The lowest attainable pressure in this system was 10^{-6} Torr by using an oil diffusion pump with a liquid N₂ trap. Indium (In) with the purity 99.9% was used as the ohmic contact material for all samples. The metallic evaporation process took about 10 minutes allowing a 300-500 Å thin metallic layer on the surface of the CdSe thin film.

The electrical measurements were carried out by soldering insulated copper wires to the evaporated indium contacts by using indium. The ohmic behaviour of the contacts was checked by the linear variation of the current voltage characteristics that is independent of the reversal of the applied bias.

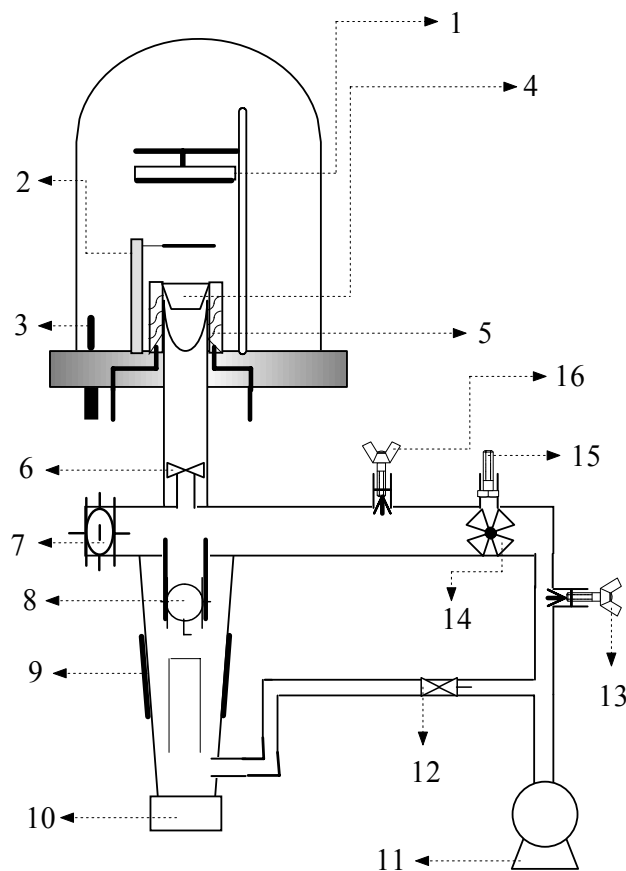


Figure 3-5: Illustration of the metallic evaporation system. 1. Substrate holder, 2. Shutter, 3. Heater current leads, 4. Source boat, 5. Filament current wire, 6. Baffle, 7. Ventilation valve, 8. Liquid Nitrogen trap, 9. Water-cooling element, 10. Diffusion pump, 11. Mechanical pump, 12. Fine valve, 13. Pirani gauge, 14. Roughing valve, 15. Pressure switch, 16. Penning gauge.

3.3 Structural Characterization

X-ray diffraction technique was used to specify the structural parameters, the existent phases and the orientation of as-grown and annealed polycrystalline CdSe thin films. The X-ray diffraction measurements were performed by using a Rigaku Miniflex X-ray diffraction system equipped with $\text{CuK}\alpha$ radiation of average wavelength 1.54059 \AA . All X-ray diffractograms were taken with the same parameters, such as, 2θ is in between 5° and 90° and scan speed of 2 degree/min . Also higher resolution measurements with smaller scan speed (0.25 deg/min) have

been taken between 25° and 27°. High resolution measurements have been used to estimate grain size by using Scherrer method. The peak matching analysis was made by using the computer software and database of X-ray diffraction system.

3.4 Electrical Measurements

The investigation of the electrical properties of the deposited CdSe thin films includes the temperature dependence of the dark resistivity and mobility of CdSe thin films with the standard dc-measurement technique applied on the prepared Hall-bar samples and van der Pauw method on the van der Pauw samples. To increase the accuracy of measurements and provide standard measurement conditions several control programs has been developed using LabVIEW graphical development software. Most of the electrical measurements have been performed by a computer using those control softwares. The temperature dependence of the dark resistivity and mobility were carried out in the temperature range of 80-400 K by means of a Janis Liquid Nitrogen VPF Series Cryostat, as shown in Fig. 3.6. The temperature of the samples inside the cryostat was measured with a GaAlAs diode sensor and controlled by a LakeShore-331 temperature controller. The vacuum inside the cryostat was achieved by the help of Ulvac Rotary pump. Cooling of the system was performed by adding liquid nitrogen to the trap through the fill port. After the addition of the liquid nitrogen, the temperature of the sample cools down to 80 K and then was gradually increased by 10 K steps to perform the required measurements.

3.4.1 Resistivity Measurements

The electrical measurement reliability strongly depends upon the ohmic behaviour of the metal contacts. The I-V plots on log-log scale were found to be linear with a slope of almost unity and symmetrical with the reversal of the current in the entire temperature range studied, indicating the ohmic behaviour of the contacts. The experimental set-up for the resistivity measurements of Hall-bar type samples is given in Fig. 3.7a. A constant current was applied between two end contacts (1 and 5) by using a Keithley 220 programmable current source and the voltage drops across the contacts (1 and 5) were measured by using a Keithley 2001 electrometer. The

range for the applied current varies from sample to sample in accordance with the total resistances they have.

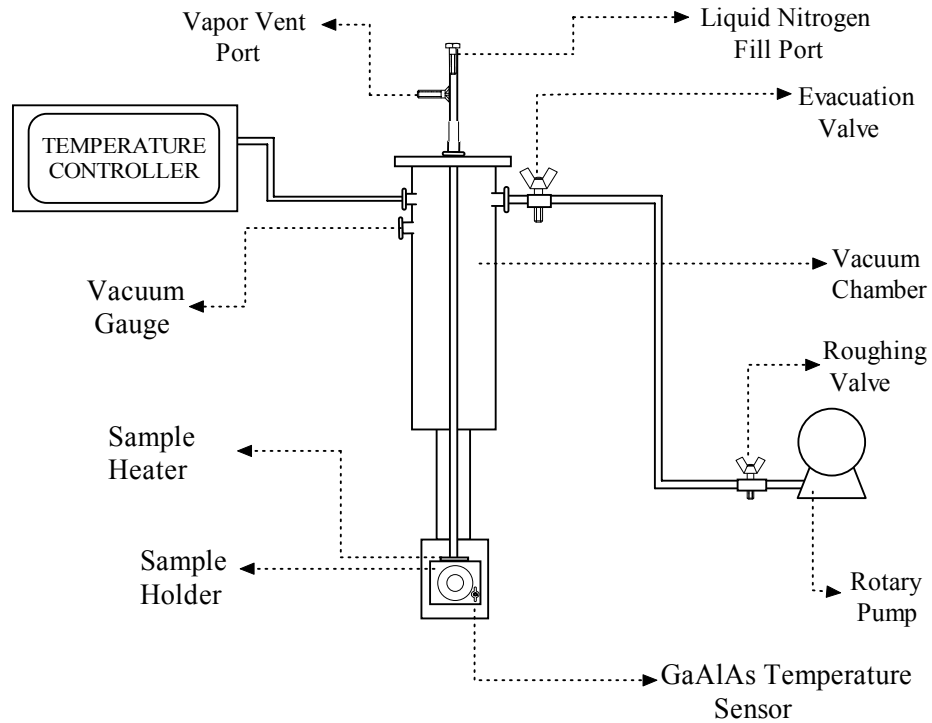


Figure 3-6: Illustration of the liquid nitrogen, sample-in-vacuum type cryostat.

The electrical resistivity expression for the sample can be written as;

$$\rho = \frac{wt}{L} \frac{V}{I} \quad (3.4.1)$$

where w is the width, t is the thickness, L is the spacing of the contacts across which the voltage is measured and V/I is the inverse slope of the I-V characteristics.

The sample dimensions and the electrode spacing were measured by using a travelling microscope having an error of $\pm 10 \mu\text{m}$. The measured total length, width and electrode spacings of the film were 1.72 cm, 0.25 cm and 1.34-0.28 cm, respectively. The possibility of a malfunctioned contact was checked by comparing

the measured voltage drops across different contact pairs with their measured transverse voltage drops.

van der Pauw technique which is illustrated in Fig. 3.7b is the most accurate method to measure the resistance of thin films. van der Pauw method has advantage to eliminate number of spurious voltages compared to dc method discussed above. Two important error eliminated with this method are imperfect alignment and thermoelectric voltage generated by the thermal gradient between probes. Table 3.1 gives a list of voltages measured for this method. The current supplied by a Keithley 220 programmable current source, and voltage was measured by a Keithley 2001 multimeter. Keithley 619 Multimeter has been used to measure the voltage between the current probes in order to reprogram the current source for supplying highest possible current without exceeding the voltage limit.

Table 3-1: Measured voltages for van der Pauw method.

Voltage Designation	Current Applied Between	Voltage Measured Between
V ₁	1-2	3-4
V ₂	2-1	3-4
V ₃	2-3	4-1
V ₄	3-2	4-1
V ₅	3-4	1-2
V ₆	4-3	1-2
V ₇	4-1	2-3
V ₈	1-4	2-3

Once the voltages listed in table 3.1 are measured the resistivity can be calculated as follows. Two values of resistivity ρ_A, ρ_B are calculated as follows [60]

$$\rho_A = \frac{\pi}{2 \ln 2} \frac{t_s}{I} f_A (V_2 + V_4 - V_1 - V_3) \quad (3.4.2)$$

$$\rho_B = \frac{\pi}{2 \ln 2} \frac{t_s}{I} f_B (V_6 + V_8 - V_5 - V_7) \quad (3.4.3)$$

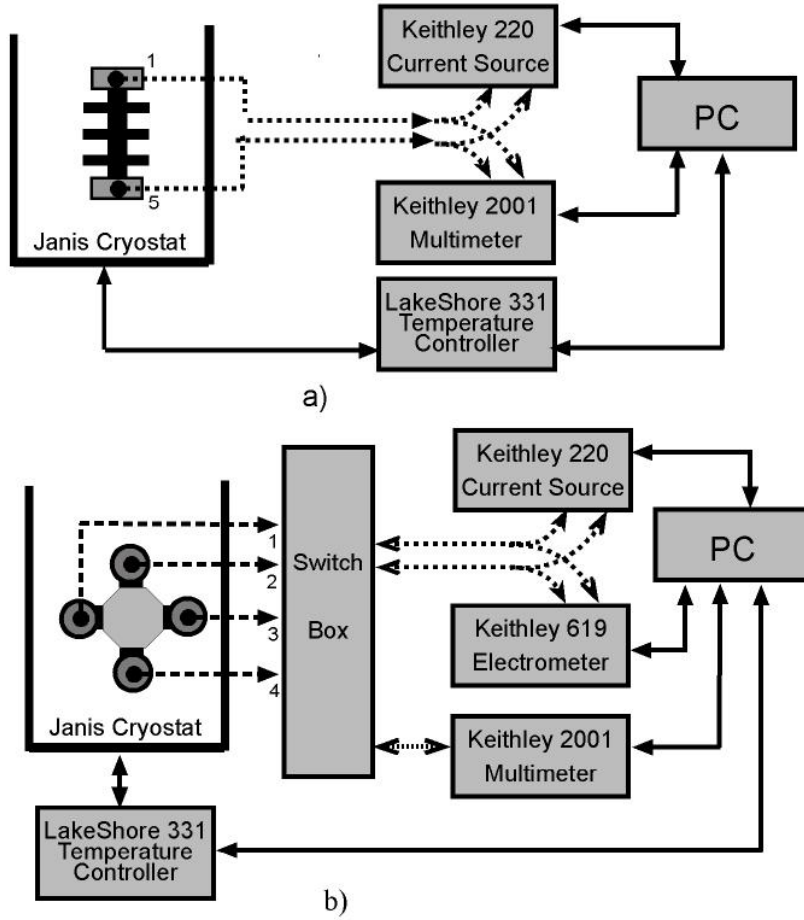


Figure 3-7: Experimental arrangement for resistivity measurements a) Hall-bar samples b) van der Pauw samples

where ρ_A, ρ_B are resistivities in ohm-cm, t_s is the sample thickness in cm, I is the current through the sample in amperes, f_A, f_B are geometrical factors based on sample symmetry, and are related to the two resistance ratios Q_A, Q_B as shown below ($f_A = f_B = 1$ for perfect symmetry).

$$Q_A = \frac{V_2 - V_1}{V_4 - V_3} \quad Q_B = \frac{V_6 - V_5}{V_8 - V_7} \quad (3.4.4)$$

Q and f are related as follows:

$$\frac{Q-1}{Q+1} = \frac{f}{0.693} \operatorname{arc} \cosh \left(\frac{\exp(0.693/f)}{2} \right) \quad (3.4.5)$$

Note that if ρ_A and ρ_B are not within 10% of one another the sample is not sufficiently uniform to determine resistivity. Once ρ_A and ρ_B are known, the average resistivity ρ_{AVG} can be determined as follows:

$$\rho_{AVG} = \frac{\rho_A + \rho_B}{2} \quad (3.4.6)$$

3.4.2 Hall Effect Measurements

The Hall effect measurements were carried out on both Hall-bar and van der Pauw type samples by dc-method. In general, the applicability of this method is taken into consideration when the sample resistance is the range of 10^3 - 10^9 ohms. AC-method is the suitable one for lower-resistive samples in application [43]. The same circuit design as in Fig. 3.7a was used for Hall effect measurements of Hall-bar samples with an applied magnetic field perpendicular to the current and the sample surface. Walker Magnion Model FFD-4D electromagnet was used for producing the magnetic field. Strength of applied magnetic field was kept constant (about 1 T) in all measurements. The current supplied by a Keithley 220 programmable current source between contacts 1 and 5. The induced Hall-voltage was measured between the contacts 3 and 7, by using a Keithley 2001 multimeter. For Hall-bar samples, the measurements were made by a series of readings with the consideration of various combinations of the magnetic field directions and the current values and directions to eliminate unwanted voltages producing errors during the measurements, such as, Ernest voltage, Ettingshausen voltage, Nernst voltage, thermoelectric voltage, and contact voltage. Table 3.2 gives a list of voltages measured for this method.

By taking all the combinations of magnetic field and current into account, Hall voltage (V_H) can be calculated from the relation;

$$(V_1 + V_4 - V_2 - V_3)/4 = V_H \quad (3.4.6)$$

and

$$V_H = \frac{IBR_H}{t} \quad (3.4.7)$$

where $R_H = 1/ne$ is Hall coefficient. The plot of IB versus V_H curve should have a slope of t/R_H from which the electron concentration n is calculated.

Table 3-2: voltage measurements for Hall-bar samples.

Voltage Designation	Current Applied Between	Magnetic Field Direction
V ₁	1-5	+
V ₂	1-5	-
V ₃	5-1	+
V ₄	5-1	-

For van der Pauw samples, the Hall effect measurements were done together with the resistivity measurements using a control software. The experimental set-up for van der Pauw samples is shown in Fig. 3.8. 12 measurements have been taken to determine the hall voltage in each temperature step. Measured voltages have been given in Table 3.3

Once the voltages are measured, two hall coefficients, R_{HC} and R_{HD} have been calculated as follows:

$$R_{HC} = \frac{2.5 * 10^7 t_s}{BI} (V_2 - V_1 + V_5 - V_6) \quad (3.4.8)$$

$$R_{HD} = \frac{2.5 * 10^7 t_s}{BI} (V_4 - V_3 + V_7 - V_8) \quad (3.4.9)$$

where R_{HC} and R_{HD} are Hall coefficients in cm^3/C , t_s is the sample thickness in cm, B is the magnetic flux, I is the current in Amperes. Similar to the van der Pauw resistivity measurements R_{HC} and R_{HD} should be within 10% of one another, in a sufficiently uniform sample. Finally average Hall Coefficient and the Hall mobility can be calculated as follows:

$$R_{H\text{AVG}} = \frac{R_{HC} + R_{HD}}{2} \quad (3.4.10)$$

$$\mu_H = \frac{|R_{H,AVG}|}{\rho_{AVG}} \quad (3.4.11)$$

where μ_H is the Hall mobility in $\text{cm}^2/\text{V}\cdot\text{s}$ and ρ_{AVG} is the average resistivity in $\Omega\cdot\text{cm}$, found with van der Pauw resistivity measurement.

Table 3-3: Hall -voltage measurements for van der Pauw samples.

Voltage Designation	Magnetic Flux	Current Applied Between	Voltage Measured Between
V ₁	+B	1-3	4-2
V ₂	+B	3-1	4-2
V ₃	+B	2-4	1-3
V ₄	+B	4-2	1-3
V ₅	-B	1-3	4-2
V ₆	-B	3-1	4-2
V ₇	-B	2-4	1-3
V ₈	-B	4-2	1-3
V ₉	0	1-3	4-2
V ₁₀	0	3-1	4-2
V ₁₁	0	2-4	1-3
V ₁₂	0	4-2	1-3

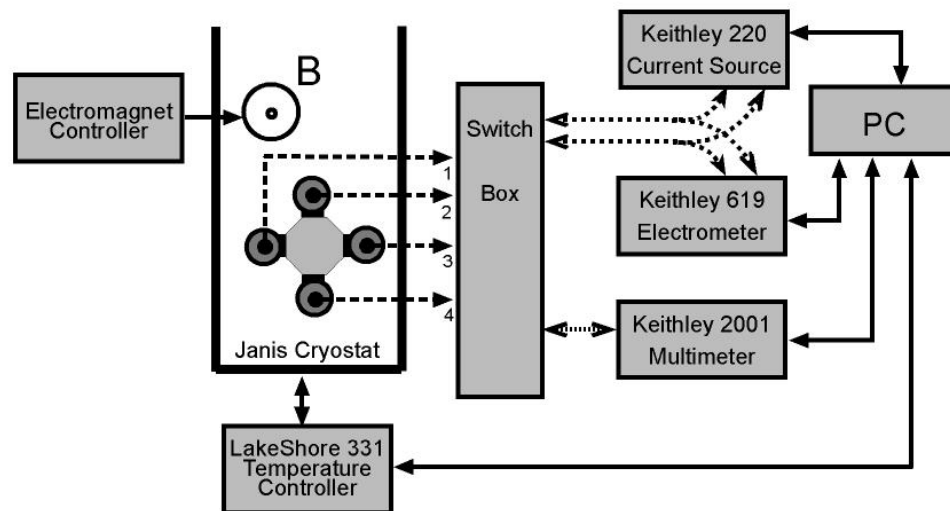


Figure 3-8: Experimental arrangement for Hall effect measurements for van der Pauw geometry.

3.5 Photoconductivity

The photoconductivity measurements were performed inside the Janis cryostat equipped with a cooling system by means of liquid nitrogen between the temperature range of 80-400 K. Photoconductivity characterization of the samples was carried out in two ways.

- a) Photocurrent under different illumination intensities, temperatures and bias voltages has been measured.
- b) Photocurrent under different illumination wavelengths, temperatures and bias voltages has been measured.

In the first type measurements samples were illuminated by using a 12-watt halogen lamp of relatively large illumination spectrum. The lamp was placed at a height of about 0.5 cm above the sample to provide a homogenous illumination on the whole surface. The illumination intensity of the lamp was changed by changing the current passing through the lamp in the range of 50-90 mA with 10 mA steps. ILFORD 1700 Radiometer was used to determine the illumination intensity values for the lamp at different applied currents. Table 3.4 gives measured illumination intensities for given current values.

Table 3-4: Illumination intensity of the halogen lamp for given current values.

Lamp Current (mA)	50	60	70	80	90
Illumination Intensity mW/cm ²	17	34	55	81	113

For illumination intensity dependent photoconductivity measurements lamp current is supplied by Keithley 220 programmable current source. Bias voltages are applied by Keithley 2400 Sourcemeter and current was measured by the same device. Experiment was completely automated by using a LabVIEW program. Control software has provided standardization in illumination time and decreased experimental errors significantly. In each temperature step first dark current has been measured. Following the dark current photocurrent data were taken at five different

light intensities. The light intensity dependent photocurrent data was used to determine the type of the recombination process which gives information about the statistical distribution of the traps inside the energy band gap. Fig. 3.10 gives the experimental setup for this measurement.

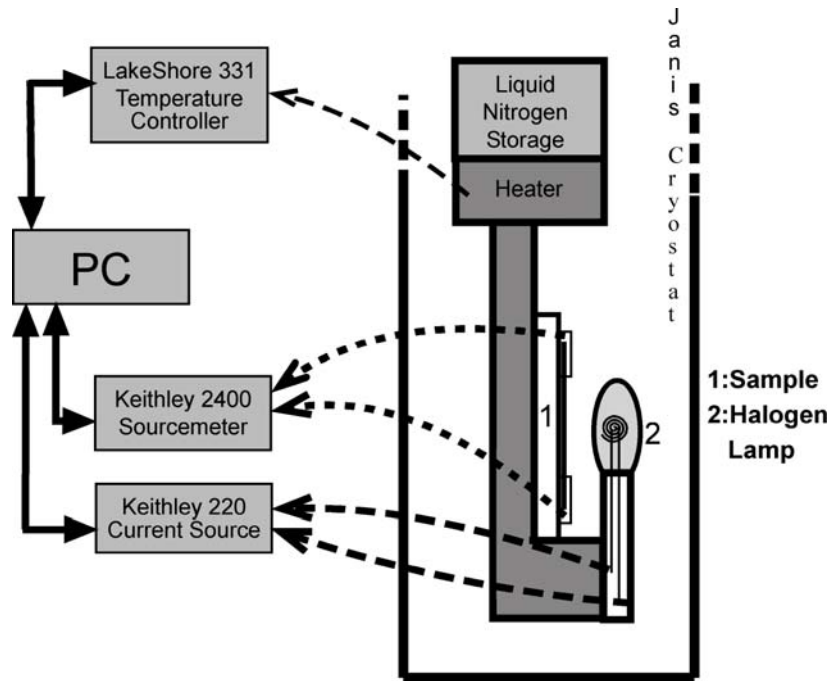


Figure 3-9: Experimental setup for the measurements of photoconductivity.

Photoresponse of the samples to illumination at different wavelengths has been measured under several bias voltages in a temperature range between 100-400K. A 150 watt halogen lamp was used as a light source. Light bundle has been focused on a Oriel MS257 monochromator which has a 1200 lines/mm diffraction grating. A shutter has been placed between the lamp and the monochromator to control the illumination cycle. Outgoing monochromatic light is directed to the sample kept under vacuum behind the quartz optical window of Janis cryostat. Voltage bias is applied by HP 4140 picoammeter and the photocurrent is measured with the same device. All of the measurement controlled with a computer

software. Fig. 3.10 gives the experimental setup for this measurement. Wavelength dependence of illumination intensity has been measured with a Newport radiometer and given in Fig. 3.11.

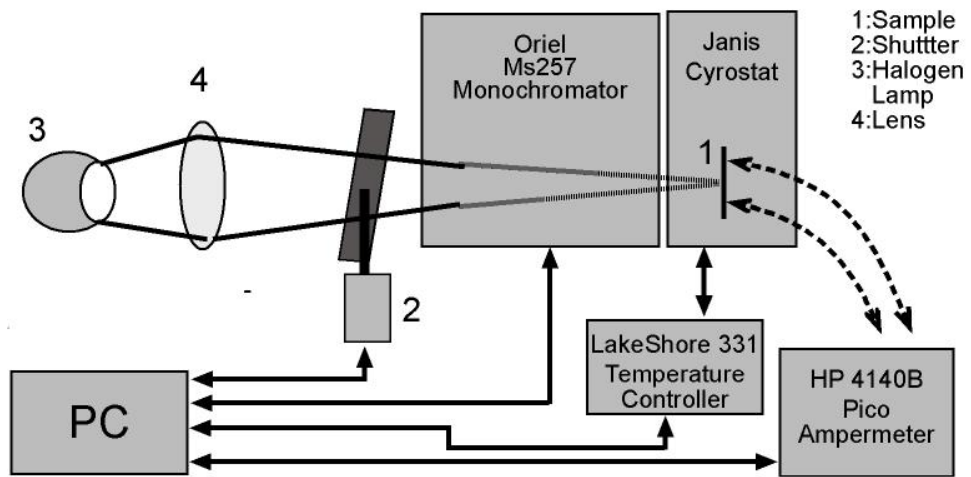


Figure 3-10: Experimental setup for wavelength dependent photoconductivity measurements.

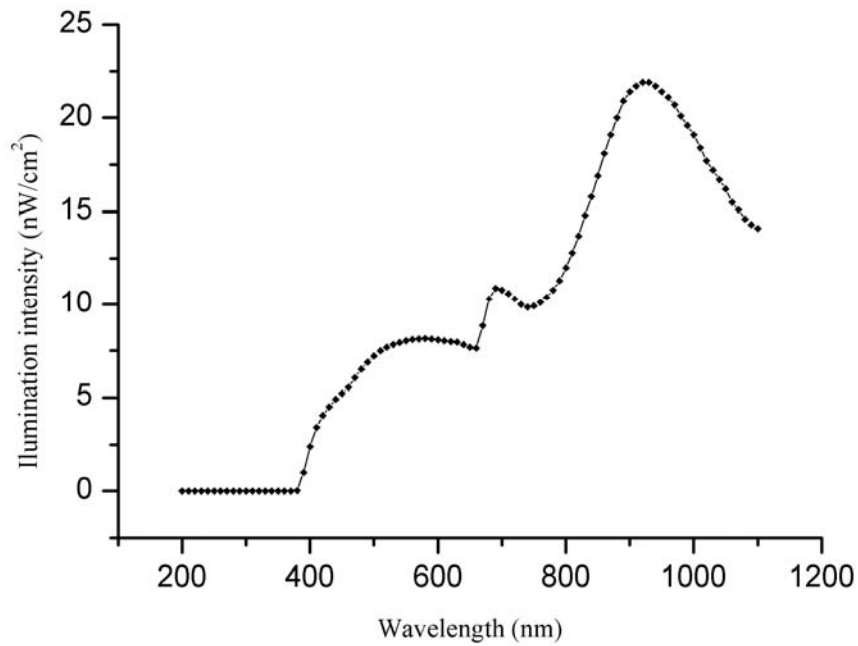


Figure 3-11: The illumination intensity - wavelength dependence of the halogen lamp-monochromator system output used in the wavelength dependent photoconductivity measurements.

3.6 Optical Measurements

Optical transmission spectrum of CdSe thin films has been examined for incident light wavelengths between 325 nm and 1150 nm at room temperature. Measurements have been taken with Pharmacia LKB Ultrospec III UV-VIS spectrometer for 325-900 nm region and with Bruker Equinox 55 FT-IR-NIR spectrometer in 600-1150 nm region. Background correction for the glass substrate has been performed in each measurement. Transmission spectrum has been used to determine optical bandgap value and type as discussed in section 2.5.

CHAPTER 4

RESULTS AND DISCUSSION

4.1 Introduction

In this chapter, the results of structural, optical and electrical measurements carried out for the characterization of the unimplanted and boron implanted CdSe thin films are presented. Relevant discussions of these results with the consideration of the effects of deposition method, deposition conditions, post annealing and B implantation on the material properties are carried out.

The structural and compositional analyses are given in the first section of this chapter. In the second section, optical measurements focusing on the investigation of optical energy gap is presented. The results obtained from the electrical measurements, namely, the temperature dependent values of conductivity, carrier density and mobility parameters studied in the temperature range of 80-400 K are discussed in the third section. Finally, the photoexcitation intensity and wavelength dependent photoconductivity properties of the CdSe thin films have been given in the fourth section of this chapter. Samples are named due to the evaporation cycle they have been deposited. Deposition parameters for the samples have been given in Table 4.1 and abbreviations given in this table are used through the whole chapter.

4.2 Structural and Compositional Characterization

To investigate the influence of growth method, growth parameters and post annealing conditions on the structural, morphological and compositional properties of CdSe thin films, X-ray diffraction (XRD), energy dispersive X-ray microanalysis (EDXA), X-ray photoemission spectroscopy (XPS) studies has been performed.

Table 4-1: Summary of deposition parameters of samples

Sample Name	Evaporation Technique	Substrate Temperature (C ^o)	Thickness (μm)
T1	Thermal	147	2.45
T2	Thermal	192	0.8
T3	Thermal	30	1.1
E1	e-beam	146	1.16
E2	e-beam	195	0.76
E3	e-beam	204	0.8

4.2.1 EDXA Results

EDXA studies has been performed for e-beam evaporated (E3) and thermally evaporated (T3) CdSe thin films in order to investigate the Cd / Se ratio and impurity content. The results have showed that the stoichiometric composition of the source material has not been perturbed too much during the deposition. It has been found that films grown on cold substrate with thermal evaporation have atomic concentrations of 49.15% Se and 50.85% Cd, while films grown with e-beam evaporation at a substrate temperature of 200° C have a composition of 49.23% Se and 50.77% Cd. No impurity content has been observed in EDXA pattern of as grown films.

Effects of annealing in N₂ atmosphere and under vacuum (<10⁻³ Torr) has also been studied on T3 type samples. Therefore, the composition of the CdSe changed slightly with annealing owing to loses of more volatile selenium. Atomic percentage concentration of Se in the films has decreased from 49.15% to 48.51% after a series of annealing process in N₂ atmosphere ending with an annealing at 400°C for 30 minutes. The ratios have decreased to 49.10 / 50.90 and 48.46 / 51.54 for films annealed under vacuum at 250° C and 500° C respectively. It is expected that re-evaporation of selenium is less significant compared to other Se composites like InSe [59] since all possible crystallization phases of CdSe thin films have 1/1 atomic ratio. As result of this EDXA studies, one can see that vacuum condition does

not assist the re-evaporation of selenium but prevents the contamination of impurities. C, O and Na peaks appearing for films annealed in N₂ atmosphere whereas not observable in the EDXA patterns of the films annealed under vacuum. EDXA patterns have been given in Fig. 4.1.

4.2.2 XRD Measurements

As discussed in section 2.2.1 CdSe like the other II-VI compounds is dimorph at ordinary pressures and crystallizes either as sphalerite structure with space group $F\bar{4}3m$ or as wurtzite structure with space group P_3mc . The energy difference is only a few meV per atom so when the samples are prepared at temperatures higher than 95°C which is the critical temperature for cubic-to-hexagonal transition, the wurtzite structure is retained at room temperature.

It is known that CdSe thin film may grow with either cubic or hexagonal structure similar to the CdSe single crystals [61]. In this study, XRD technique is used to determine the phases present and the orientation of polycrystalline CdSe thin films deposited by thermal evaporation and e-beam evaporation techniques. XRD measurements have been performed following to each annealing process in order to observe the possible changes in crystal structure.

The XRD spectra has revealed that the CdSe films deposited at different substrate temperatures have polycrystalline structure and post depositional heat treatments did not alter the structure of as-grown film remarkably. Furthermore, identification of the appearing crystalline peaks confirmed that both of the cubic and hexagonal phases of CdSe exist in all of the deposited films. Peak positions and relative intensities are in a very good agreement with the IDDC database and previous works [25, 62-63]. No additional peak which does not belong to one of those phases exists in diffractograms. This result shows that Se/Cd ratio is very close to 1 and in agreement with EDXA results.

All of the XRD diffractograms has a single major peak at $2\theta \cong 26.1^\circ$ which indicates the preferred orientation of films are $002_{\text{hexagonal}}$ (111_{cubic}) parallel to the substrate surface. Also several minor peaks whose intensities do not exceed 7% of the main peak are observed. Fig.4.2 gives the XRD diffractograms of as-grown CdSe

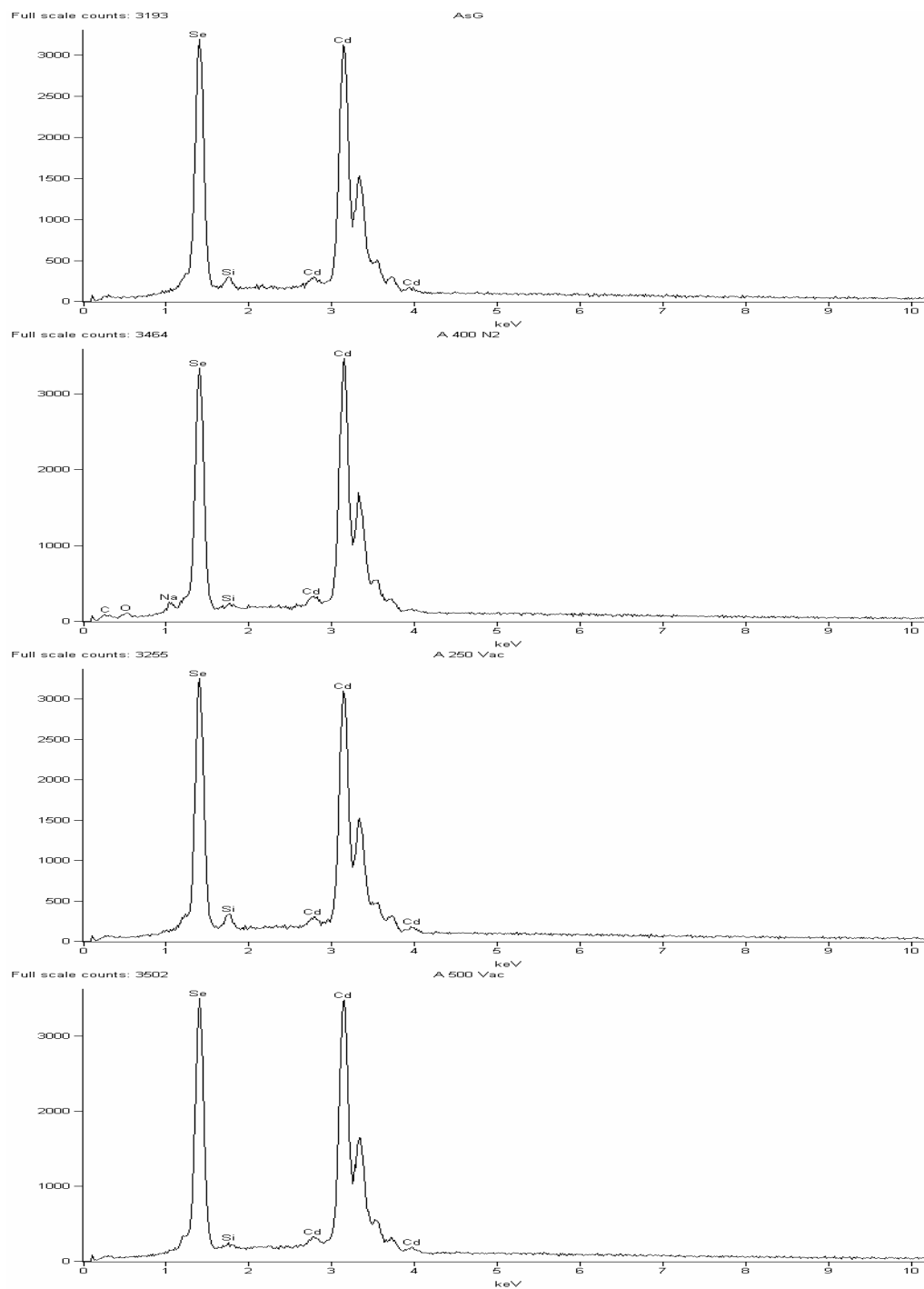


Figure 4-1: EDXA patterns for T3 samples a) Asgrown, b) Annealed at 400°C in N₂ atmosphere, c) Annealed at 250°C under rough vacuum, d) Annealed at 500°C under rough vacuum.

thin films deposited under different conditions. Table 4.2 summarizes d-value, miller indexes and relative intensities of major and several minor peaks, while Table 4.3 gives a list of main peak intensities.

The crystalline sizes (D) were calculated using the Scherrer formula [64] using the full-width at half-maxima of the main peak (β)

$$D = \frac{0.94\lambda}{\beta \cos \theta} \quad (4.2.1)$$

The strain (ϵ) calculations could not be performed since the minor peaks are too small and usually could not be fitted with Gaussian distribution. Calculated grain sizes vary between 40 and 95 nm.

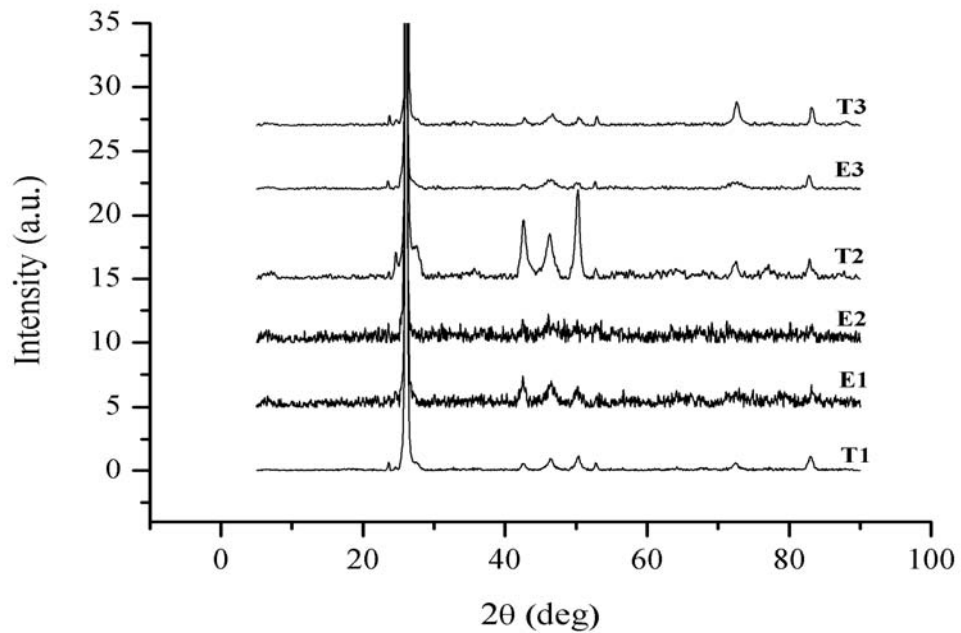


Figure 4-2: XRD diffractograms of the as-grown CdSe thin films deposited at different evaporation cycles.

Results indicate that crystallization process is directly related to deposition conditions especially substrate temperature and film thickness. For lower thickness such as in sample T2, the films have random particle orientation, identified by the

Table 4-2: Positions, properties and measured relative intensities of as-grown CdSe thin films.

Peak #	1	2	3	4	5	6	7	8	9	10
hkl	100 _h	002 _h , 111 _c	101 _h	102 _h	110 _h , 220 _c	103 _h	112 _h , 311 _c	105 _h	300 _h , 422 _c	511 _c
2θ (in deg)	23.9	25.4	27.1	35.1	42	45.8	49.7	71.9	76.8	82.4
d-value (Å)	3.72	3.51	3.29	2.254	2.151	1.98	1.834	1.312	2.24	1.169
Sample	I / I ₀	I / I ₀	I / I ₀	I / I ₀	I / I ₀	I / I ₀	I / I ₀	I / I ₀	I / I ₀	I / I ₀
T1	0.3	100	0.7	-	0.5	1	1.2	0.7	-	1.2
T2	2.6	100	2.6	0.8	4.6	3.6	7	1.4	1.1	1.6
T3	0.5	100	0.5	0.4	0.7	0.8	0.6	1.8	-	1.4
E1	1.3	100	1.2	-	2,4	2.1	1.6	1.2	1	1.3
E2	-	100	0.5	-	1.8	2.7	1.4	-	-	1
E3	0.3	100	0.7	-	0.4	0.7	0.5	0.5	-	1.1

Table 4-3: Summary of main peak intensities.

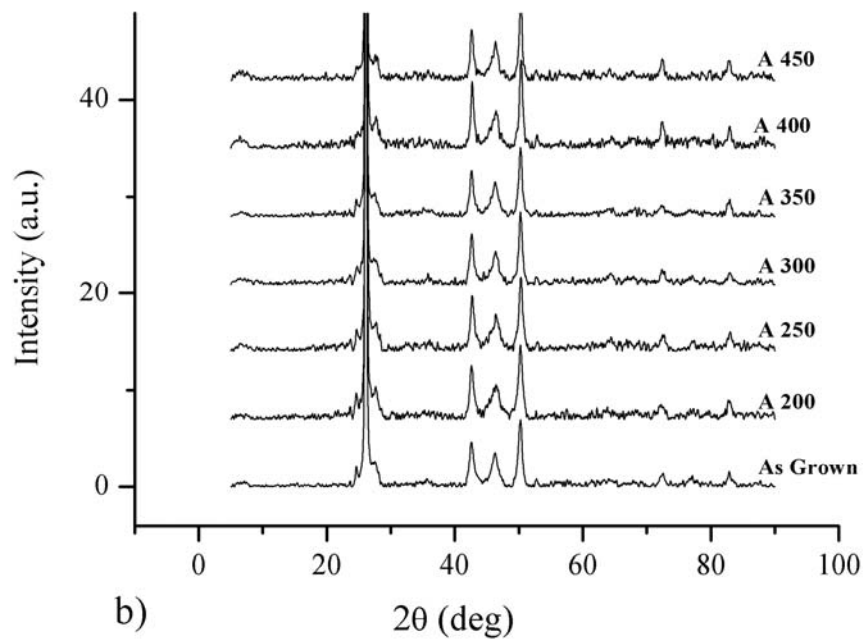
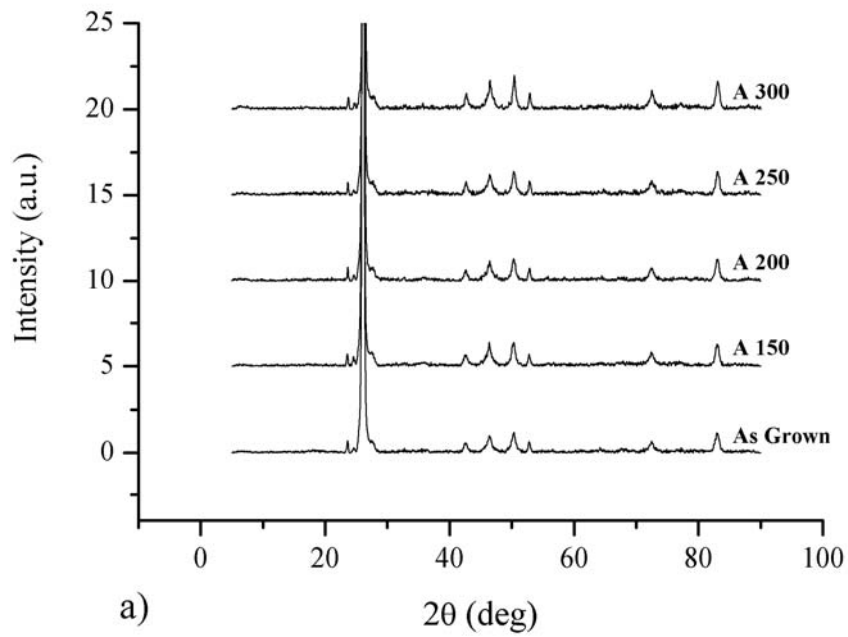
Sample	T1	T2	T3	E1	E2	E3
Main peak intensity (cont/Min)	23218	3764	12475	5114	4797	12639

presence of various peaks at (110_h), (112_h) etc., As the film thickness increases the 002_h diffraction peak becomes more and more dominant as observed in T1 samples.

These results indicate that at the initial stages of the film formation, the deposited atoms are at random orientation. As the thickness of the film increases the polycrystalline grains begin to orient mainly along (002_h) direction [29].

Post depositional annealing generally improves the polycrystalline structure of the films. Improvement occurs due to crystallization of existing amorphous phases. But it is not applicable to the films in this study. Since all of the films grow in polycrystalline structure annealing did not cause any re-crystallization. The only exception is observable in films deposited with e-beam evaporation (E3) and annealed at 450°C. In this sample (103_h) and (105_h) peaks become clearer while peaks at $2\theta = 42^\circ$ and $2\theta = 49.7^\circ$ completely disappears. Effects of annealing on XRD patterns are given in Fig. 4.3. Erskine [63] et al. has reported comparable (80-100 nm) grain sizes using the electron micrographs of surface replicas of CdSe thin films and noted that no significant grain growth occurs during annealing.

No measurable change has been found in main peak intensity and grain size for B implanted samples. Shepherd et al. [65] has reported similar results for the B-implanted CdSe thin films up to doses of 1×10^{16} ions/cm². They have also implanted Al and Cr ion into CdSe and reported significant changes in the crystallography of the films, namely a decrease in the value of the c consistent with the implanted ions occupying substitutional sites. On the other hand the smaller ionic radii of B compared to Al, Cr, Cd causes less effect in structure [65].



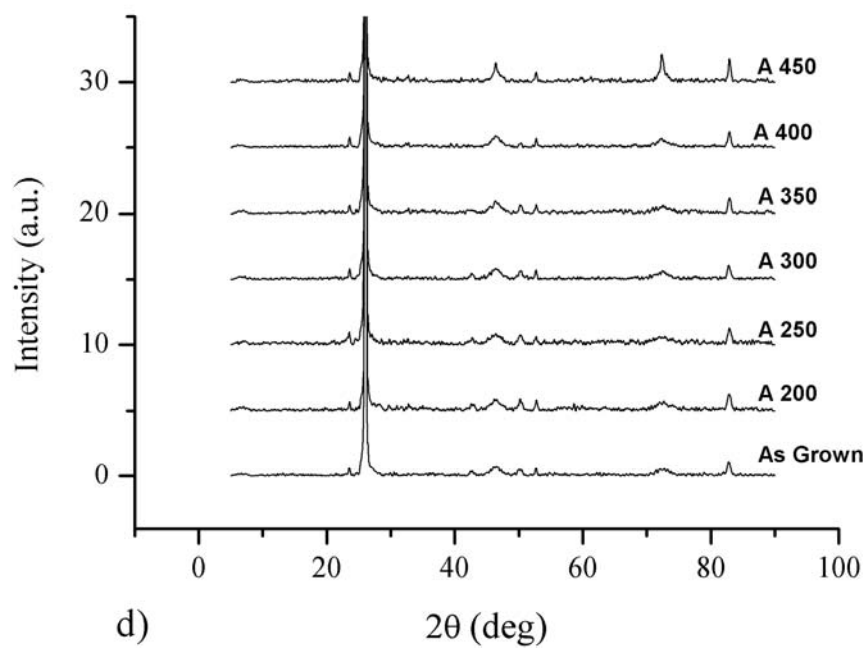
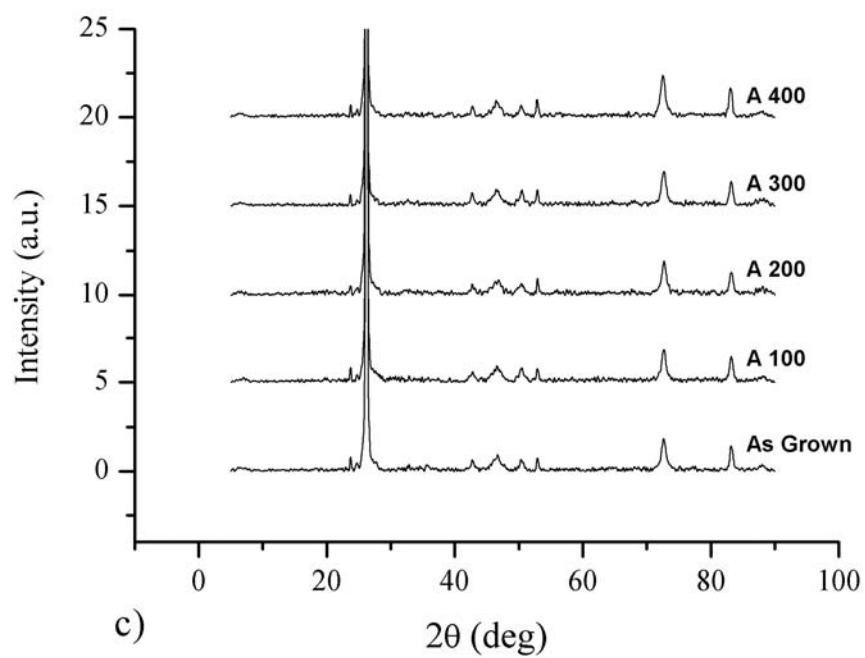


Figure 4-3: X-ray diffraction patterns of samples a) T1, b) T2, c) T3, d) E3 for different annealing levels.

4.3 Optical Characterization

The optical properties of e- beam evaporated and thermally evaporated CdSe thin films have been studied to investigate the influence of growth method, growth parameters and post annealing conditions on the optical parameters. The transmission measurements were carried out by using a Pharmacia LKB Ultrospec III UV-VIS spectrometer in the range of 325-900 nm region and a Bruker Equinox 55 FT-IR-NIR spectrometer in the range of 600-1150 nm. Figure 4.4 shows typical transmission spectra for investigated films. Interference maxima and minima due to multiple reflections on the film surfaces can easily be observed.

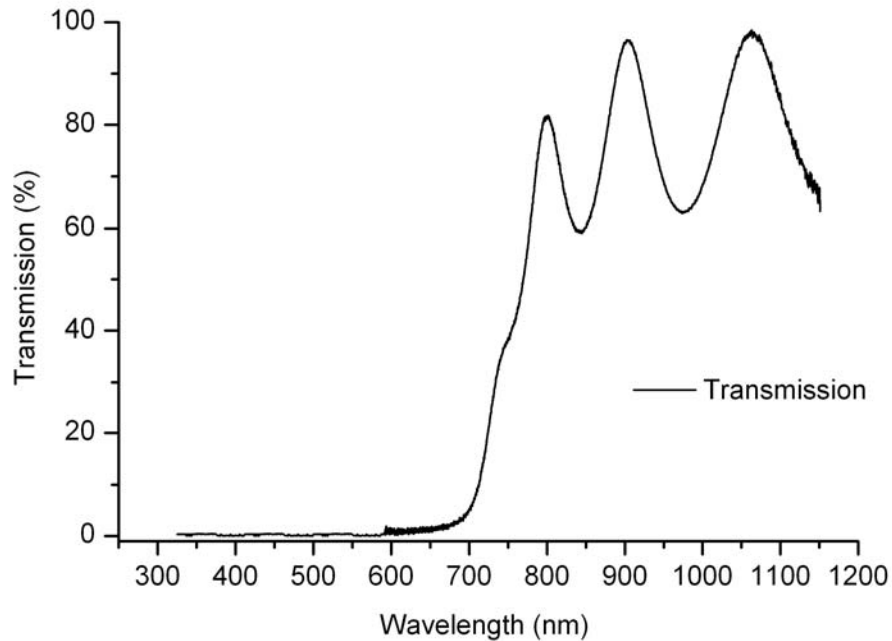


Figure 4-4: Typical transmission spectra (Sample T3 as-grown)

Although refractive index have been calculated form the transmission spectra using the Swanepoel method [66] the optical part of this work has focused on the investigation of optical energy gap of the samples.

The optical absorption coefficient has been calculated from the transmission data using the relation,

$$\alpha = \frac{1}{d} \ln \left(\frac{I}{I_0} \right) \quad (4.3.1)$$

where d is the thickness I_0, I are intensities of incident and transmitted lights, respectively. Reflection coefficient for each wavelength is also necessary to calculate the absorption coefficient sensitively. Fortunately, optical energy gap of a semiconductor material is not directly related to value of absorption coefficient but the wavelength at which transmission spectrum start to change significantly. So a constant reflection coefficient will not effect the energy band gap calculations. This assumption is not inaccurate since our interest focuses on a very narrow band of the spectrum (about 10 nm) around the fundamental absorption edge. Reflection coefficient has been taken to be zero through this study.

Variation of the optical absorption coefficient near the fundamental absorption edge has allowed us to determine the optical energy gap as discussed in section 2.5. The absorption coefficient (α) at the optical absorption edge varies with the photon energy ($h\nu$) according to the expression ;

$$(\alpha h\nu) = A(h\nu - E_g)^n \quad (4.3.2)$$

where A is a constant and E_g is the optical energy gap and n is an index having the values of $\frac{1}{2}$ for the direct allowed transition and 2 for the indirect allowed transitions. In order to determine the suitable n value $(\alpha h\nu)^{1/n}$ vs. $h\nu$ is plotted for $n = \frac{1}{2}$ and $n=2$. A typical plot is given in Fig. 4.5.

As observed from the figures, the plots for $n = \frac{1}{2}$ fit well to the expression given by equation 4.3.2. Thus, a plot of $(\alpha h\nu)^2$ as a function of $h\nu$ yields a linear portion in the region of strong absorption near the absorption edge, indicating that absorption takes place through allowed direct interband transition [59]. Optical energy gap values have been obtained by extrapolating these linear portions to the $h\nu$ axis. Figure 4.6 shows the variations of $(\alpha h\nu)^2$ as a function of $h\nu$ for all of the as-grown samples and Table 4.4 gives the calculated optical energy gap values for these samples.

Table 4-4: Optical band gap energies of as-grown samples.

Sample	T1	T2	T3	E1	E2	E3
Optical band gap(eV)	1.66	1.72	1.75	1.73	1.91	1.73

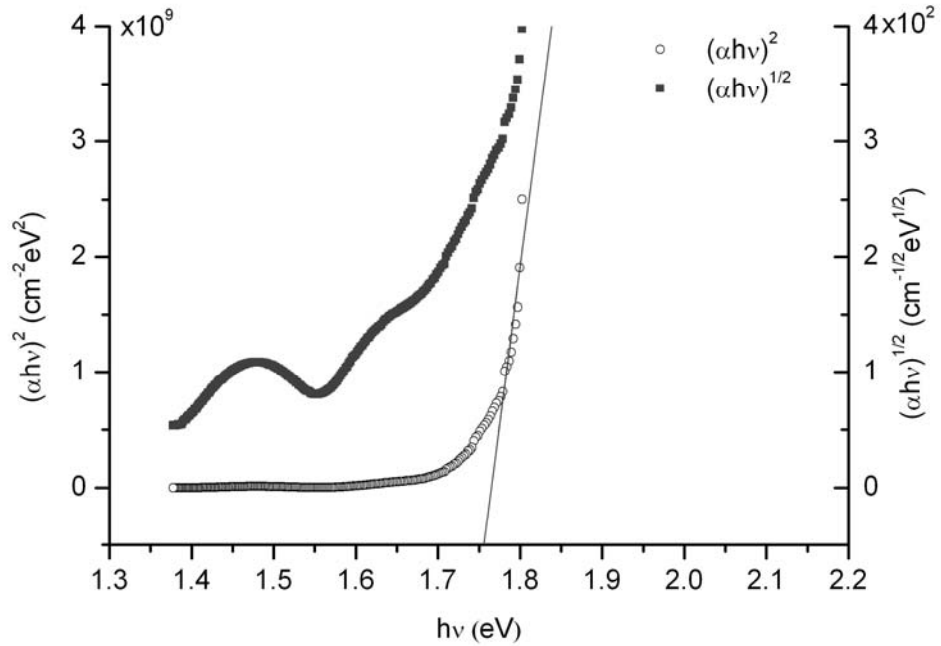


Figure 4-5: Comparison of $(\alpha h\nu)^2$ and $(\alpha h\nu)^{1/2}$ plots.

Optical band gap of all as-grown samples are 1.73 ± 0.02 eV with two expectations. First of them is T1 whose energy gap has been calculated to be 1.66 eV is four times thicker than the other samples. Very low transmission rates caused by the thickness makes the determination of absorption edge difficult and decreases the band gap. Similar observations of decrease in the band gap with increase in film thickness were reported by Velumani et al. [29], and Pal et al. [67]. The second one

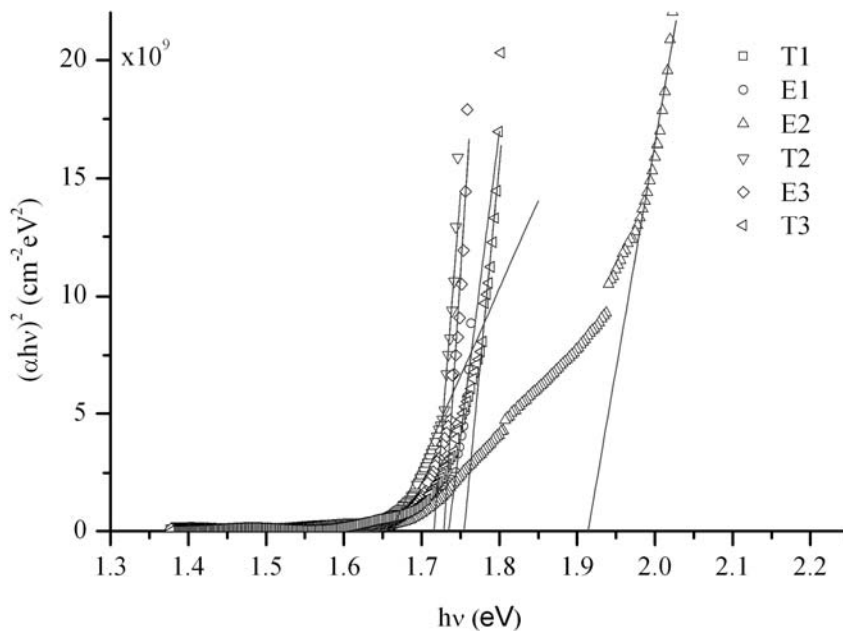


Figure 4-6: The variation of $(\alpha hv)^2$ as a function of $h\nu$ for all as grown samples.

is E2. Two different linear regions appear in this sample indicating the existence of two different direct band gap energy with $E_{g1}=1.68$ eV and $E_{g2}=1.91$ eV. The two direct transitions observed in the films may be attributed to spin orbit splitting of the valance band [29, 67, 68]. Almost the same values have been reported by Mondal et al. [69] for the CdSe films on the glass substrates.

Transmission measurements have been repeated after each annealing step for all samples. Figure 4.7 shows the variation of the optical energy gap as a function of annealing for selected samples. It is observed that annealing does not change the energy gap. Variations limited to a few meV and irregular, is caused by experimental errors. These results are in agreement with the XRD results which indicate that crystallite does not increase with annealing.

Effect of boron implantation on the energy gap has also been studied. Implantation and annealing of the implanted films did not produce any observable change in the optical energy gap. This result indicates that the boron atoms produce

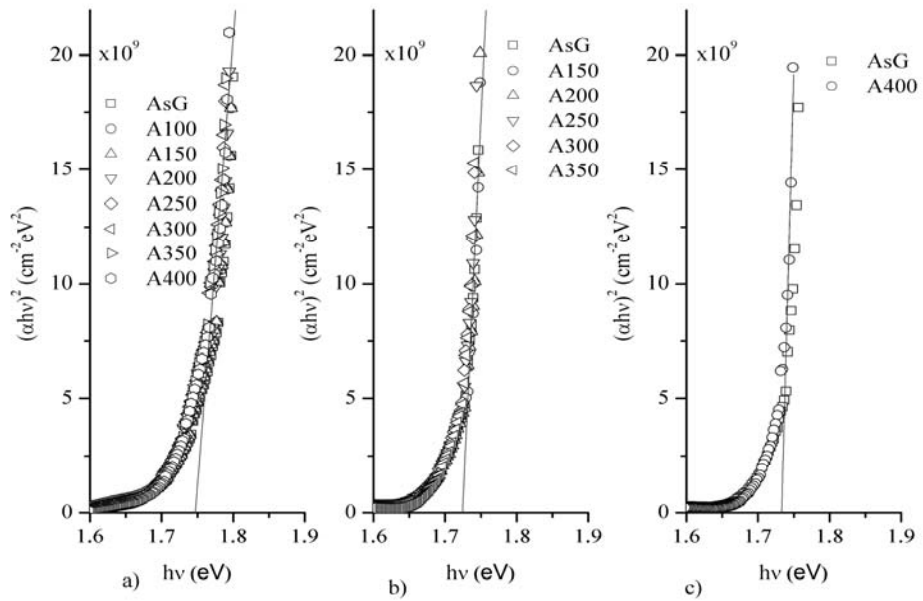


Figure 4-7: The variation of $(\alpha h\nu)^2$ as a function of $h\nu$ for selected samples. a) T2, b) T3, c) E3

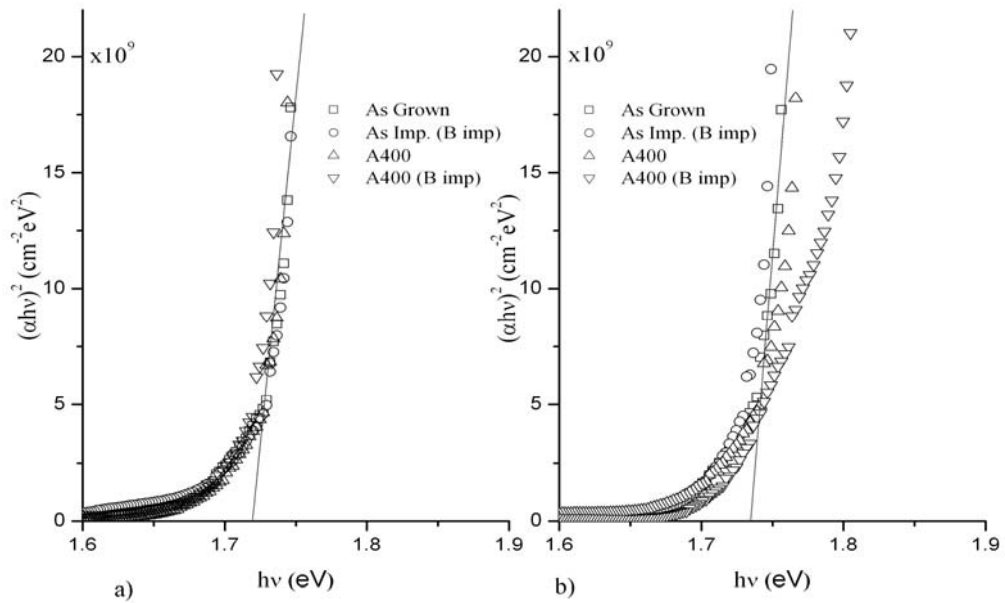


Figure 4-8: The variation of $(\alpha h\nu)^2$ as a function of $h\nu$ for as grown, as implanted and annealed samples a) T2, b) E3.

interstitial impurities and does not create additional highly populated localized states inside the energy gap. Figure 4.8 gives the $(\alpha h\nu)^2$ vs. $h\nu$ plots of as grown, as implanted and annealed samples grown with thermal and e-beam evaporations.

4.4 Electrical Characterization

In this section, the results of the electrical measurements carried out on the e-beam evaporated and thermally evaporated CdSe thin films have been presented. Dominant conduction mechanisms at different temperature regimes have been discussed and also effects of boron implantation on the conductivity of the films have been analyzed.

For the electrical measurements on the samples, indium contacts were obtained by evaporation of indium on the films using suitable masks. In the first step, the ohmic behaviors of the contacts were checked by measuring linear variation of the I-V characteristics, which was independent from the polarity of applied currents and contact combinations. A typical example for logarithmic plots of I-V is shown in Fig. 4.9.

4.4.1 Conductivity Measurements and Conduction Mechanisms

Electrical conductivity of the films has been measured with DC and van der Pauw techniques discussed in Chapter 3. Sign of the measured Hall-voltages indicated that all of the CdSe thin films exhibit n type conduction. This result corrects the EDAX measurements which had revealed the existence of excess cadmium. The room temperature conductivity of the thermally evaporated CdSe thin films vary between 10^{-3} and 10^1 ($\Omega\text{-cm}$)⁻¹. Compared to thermally evaporated ones e-beam evaporated CdSe thin films are much more resistive with conductivity values varying between 5×10^{-7} and 1.5×10^{-6} ($\Omega\text{-cm}$)⁻¹. B implanted T2 samples have a conductivity value about 5 times greater than the unimplanted ones. Very high resistivities of the e-beam evaporated films make the electrical characterization of the samples difficult, especially for the Hall-effect measurements. Room temperature

electrical parameters of the as-grown CdSe and boron implanted CdSe films has been given in Table 4.5.

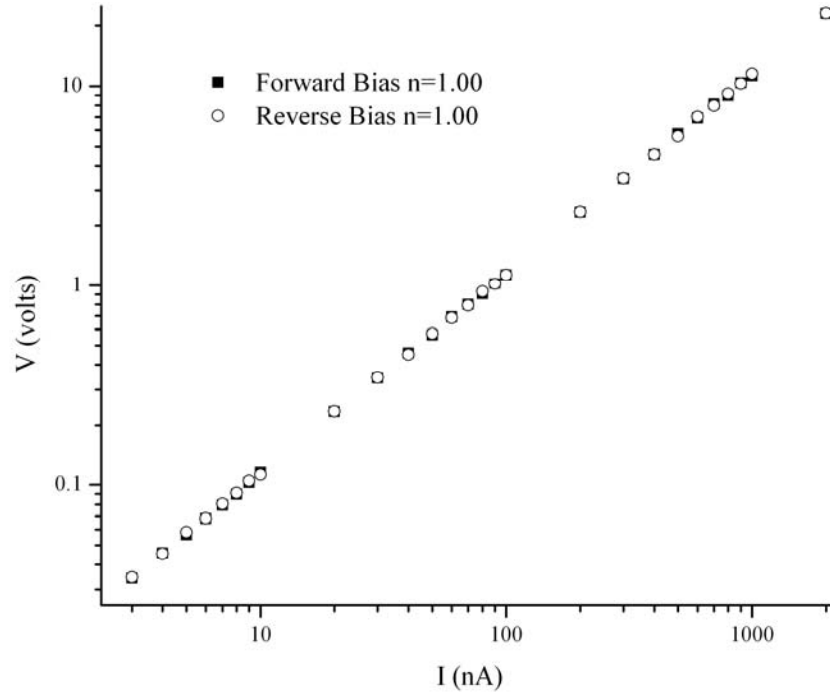


Figure 4-9: Typical I-V characteristics for CdSe thin Films with indium contacts.

Table 4-5: Summary of the conductivity, mobility and carrier density values of as grown samples at room temperature.

Sample	σ ($\Omega\text{-cm}$) ⁻¹	μ ($\text{cm}^2/\text{V-s}$)	n (cm^{-3})
T1	1.2×10^{-2}	86,8	-
T2	7.5×10^{-4}	11.8	5.9×10^{14}
T2 (B imp)	3.4×10^{-3}	18.3	1.9×10^{15}
T3	9.4	-	-
E1	1.7×10^{-6}	-	-
E2	5.2×10^{-7}	-	-
E3(B imp)	1.2×10^{-5}	-	-

The temperature dependent conductivity in CdSe thin films was measured in the temperature range of 80-400 K in order to reveal the dominant transport mechanisms and the general behavior of the conductivity. The temperature dependent conductivity of the CdSe thin films deposited with both techniques shows very similar behaviors although they have very different conductivity values. Such as, the variations of the conductivity with the temperature for both films are similar but resistivity of e-beam evaporated sample is 500 times greater than the thermally evaporated one. In both type of samples the conductivity increases very slightly between 80 and 220 K but after 220 K a very sharp exponential increase is observable. Similar behaviors are commonly observed in polycrystalline semiconductor thin films [42]. Typical temperature dependent conductivity behavior of CdSe thin films is given in Fig. 4.10.

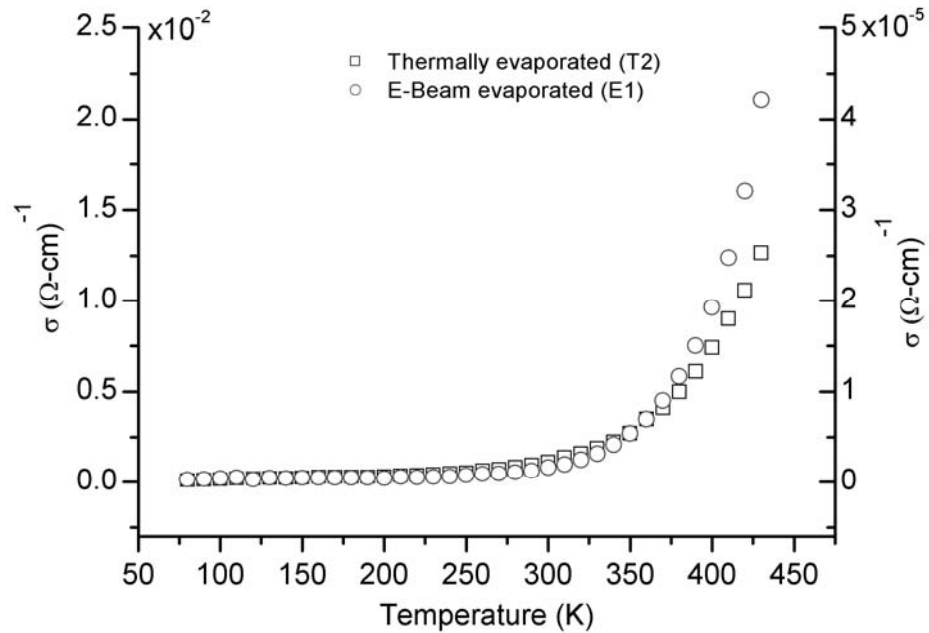


Figure 4-10: Temperature dependent conductivity of thermally evaporated (left axis) and e-beam evaporated (right axis) as grown CdSe thin films.

Transport mechanisms in the deposited films have been investigated by analyzing the temperature dependent conductivity values. The possibilities of dominant conduction mechanisms within possible conduction mechanisms as discussed in section 2.1 are studied by comparing them to each other at different temperature regions. Temperature dependent conductivity parameters proposed by these mechanisms are summarized below.

- 1) Thermionic emission over the grain boundary potential barrier.

$$\sigma\sqrt{T} = \sigma_0 \exp\left(-\frac{E_a}{kT}\right) \quad (4.4.1)$$

- 2) Thermally assisted tunneling.

$$\sigma = \sigma'_0 \left(1 + \frac{F^2}{6} T^2\right) \quad (4.4.2)$$

- 3) Hopping

$$\sigma\sqrt{T} = \sigma''_0 \exp\left[-\left(\frac{T_0}{T}\right)^{1/4}\right] \quad (4.4.3)$$

The variations of $\ln(\sigma\sqrt{T})$ as a function of inverse absolute temperature of the thermally evaporated and e-beam evaporated as-grown CdSe thin films have been given in Fig. 4.11a and b. All of the plots indicate the existence of two linear regions with a transition region between them.

At low temperatures, conductivity of the thermally evaporated samples increases slightly with activation energies between 7.5 and 17.7 meV. After 230 K conductivity starts to increase much sharply with activation energies between 50 and 233 meV. It has been observed that the conductivity of the as-grown samples increases with decreasing substrate temperature while activation energies are decreasing.

Another factor that affects the conductivity of the films is film thickness. The effective mean free path model [70] gives an expression for the thickness dependence of resistivity of polycrystalline semiconducting films as;

$$\rho = \rho_g \left(1 + \frac{3l_g(1-p)}{8t}\right) \quad \text{for } l_g/t > 0.1 \quad (4.4.4)$$

where ρ_g is the resistivity of an infinitely thick polycrystalline film, l_g is the mean free path in the corresponding film, t is the film thickness and p is the specularity parameter. Mohanchandra and Urchil [71] has found that $\rho_g=0.2$ (Ω -cm) and $l_g(1-p)=6.96 \times 10^{-6}$ (cm) for CdSe.

As mentioned earlier, the samples evaporated by e-beam show similar temperature dependent conductivity characteristics with higher resistivity and activation energy values. Conductivity results are in correlation with the XRD observations which anticipate lower crystallites and smaller grain sizes for those samples. In low temperature region below 220 K, e-beam evaporated CdSe thin films have activation energies of 7.3-10.5 meV. Their activation energy increases to 470-318 meV above 250K. Calculated activation energies for all samples are given in Table 4.6

Table 4-6: The activation energy (E_a) of as grown CdSe thin films obtained from the temperature dependent conductivity measurements. * indicates the B implanted samples.

Sample	T1	T2	T2*	T3	E1	E2	E3*
E_a (meV) in 80-230 K	17.7	16.6	5.5	7.5	10.6	7.3	7.9
E_a (meV) in 240-400K	216.5	233.1	184.0	49.5	318.0	469.8	258.8

Another part of this study was investigation of the effects of doping with boron on the structural, optical and electrical properties of CdSe thin films. For doping process ion implantation technique was used and the surface of the sample was bombarded with the ion beam of 10^{15} ions/cm² at 100 keV. Due to low implantation level structural and optical characteristics of the films has not changed considerably. On the other hand, significant changes have been observed in the conductivities of the samples. Boron implantation has decreased the activation energy of T2 sample to 184 meV and 5.5 meV in high and low temperature regions, respectively. Conductivity of the both samples increased after annealing at 250°C but drop below the as-grown values after the second annealing step at 300°C. The results

can be explained with an increase in crystallite and/or segregation of Se atoms. Fig. 4.12 is given for the comparison of the conductivity versus temperature plots for thermally evaporated (T2) as-grown and as-implanted CdSe thin films. And Fig. 4.13 is given to show the effects of annealing in these films.

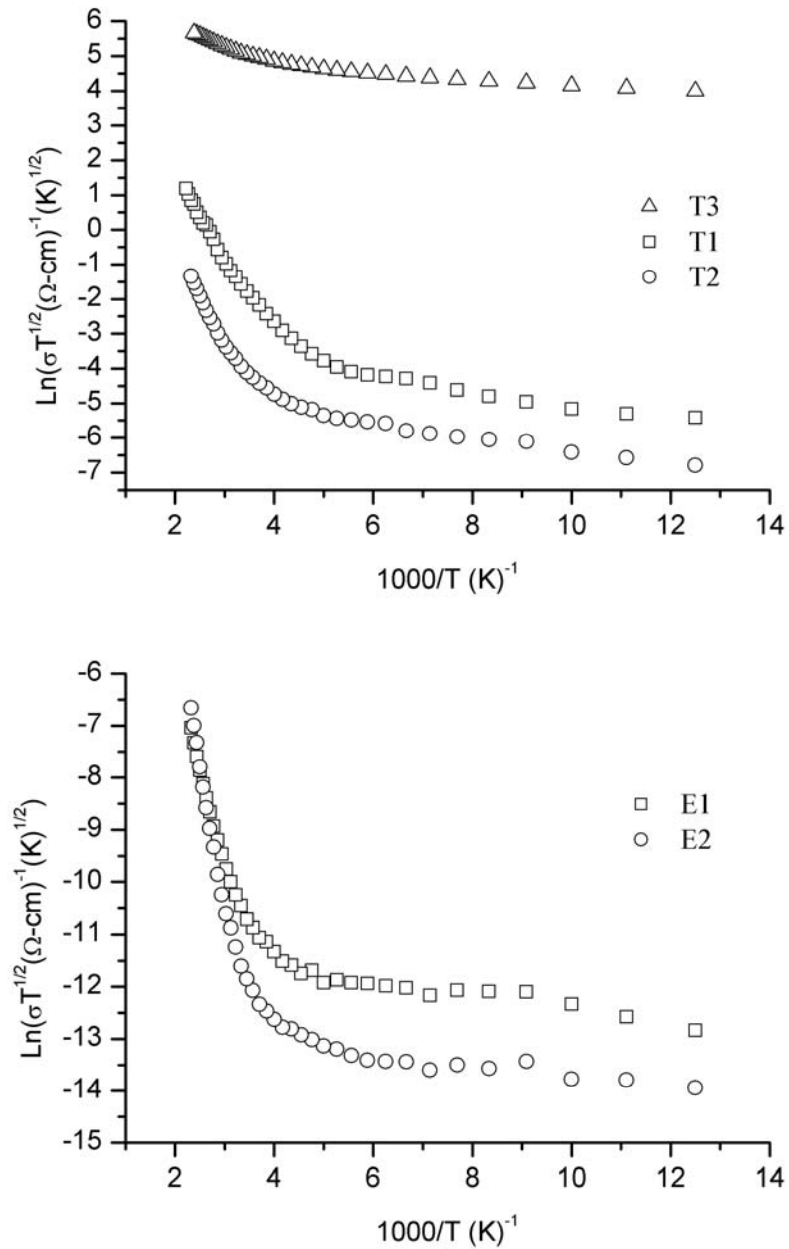


Figure 4-11: The variation of $\text{Ln}(\sigma T^{1/2})$ as a function of the inverse absolute temperature for a) thermally evaporated, b) e-beam evaporated CdSe samples.

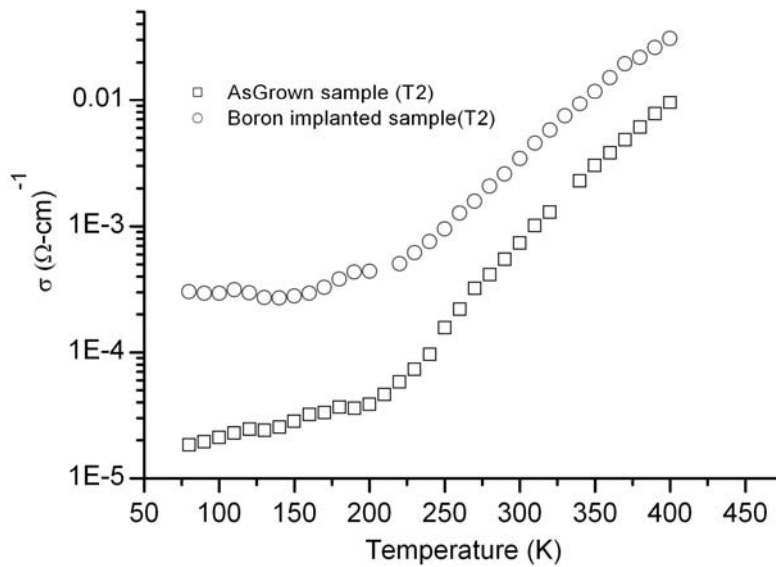


Figure 4-12: Variation of conductivity as a function of temperature for unimplanted and B implanted CdSe thin films

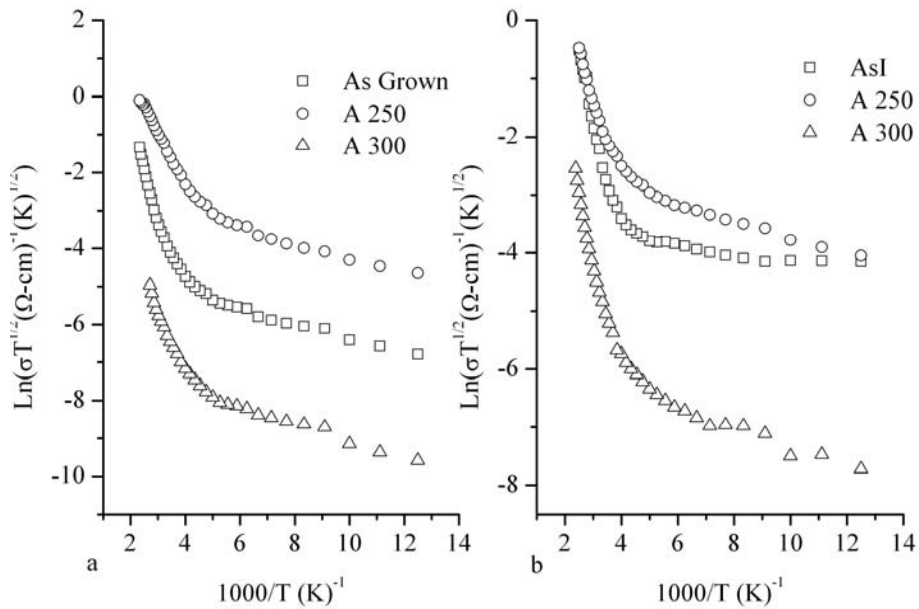


Figure 4-13: The variation of $\ln(\sigma T^{1/2})$ as a function of the inverse absolute temperature for a) unimplanted T2, b) B implanted T2 CdSe samples at various annealing temperatures.

Conductivity of the films deposited on cold substrate (T3) by thermally evaporation is significantly higher than the ones deposited on the hot substrates. This implies that increasing substrate temperature produces defective structure, whereas the disordered structure of these films is not visible in XRD measurements as it appears with electrical measurements. Resistivity and activation energies of these films increased with annealing as a result of decrease in selenium ratio and defects in structure, respectively.

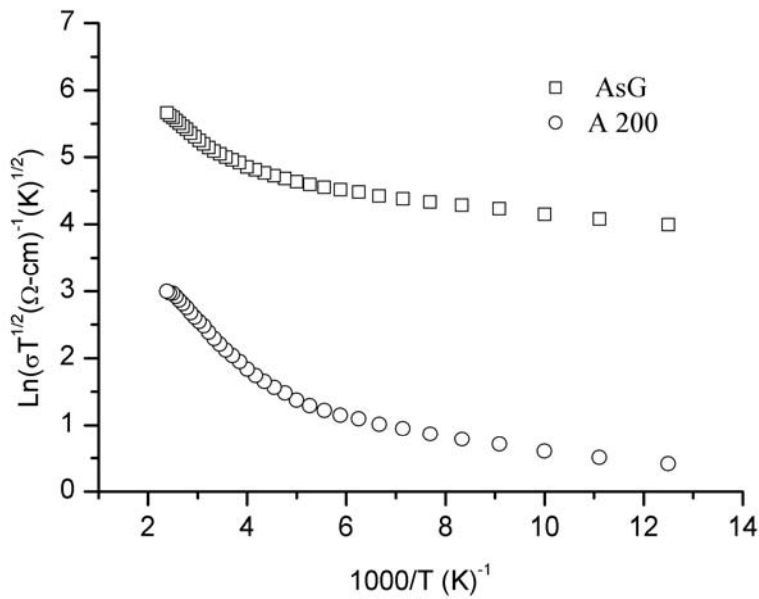


Figure 4-14: The variation of $\ln(\sigma T^{1/2})$ as a function of the inverse absolute temperature for T3 samples.

The variation of activation energy implies that different conduction mechanisms take place in different temperature regions. For all of the samples, the thermionic emission of the carriers above the grain boundary is the dominant conduction mechanism above 250 K. Experimental results fit very well with the models discussed in section 2.3.1. A more detailed analysis of the conductivity-temperature data was required to find the dominant conduction mechanisms at low

temperature region. $\sigma - T^2$ and $Ln(\sigma T^{1/2}) - T^{-1/4}$ graphs corresponding to thermally assisted tunneling and variable range hopping, respectively, have also been plotted for each measurement in order to compare the models with experimental data. As shown in Fig. 4.10 a-c, $Ln(\sigma T^{1/2}) - T^{-1/4}$, $\sigma - T^2$, and $Ln(\sigma T^{1/2}) - 1000/T$ plots show linear behaviors in the temperature region 80-160 K, 170-240 K and 250-420 K, respectively. The temperature regions may change by an amount of ± 20 K for different samples grown with thermal evaporation.

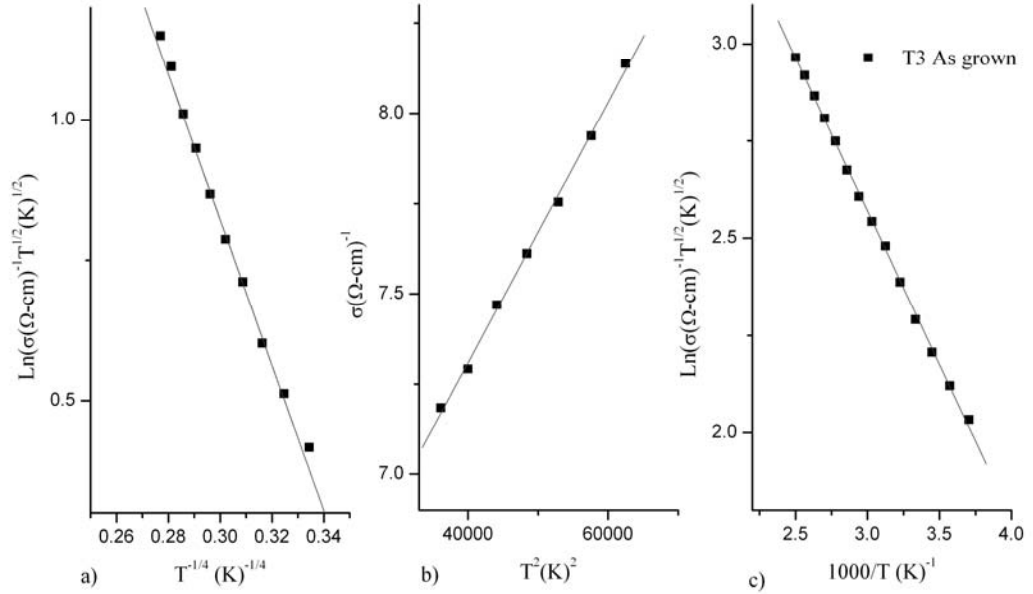


Figure 4-15: a) $Ln(\sigma T^{1/2}) - T^{-1/4}$, b) $\sigma - T^2$, and c) $Ln(\sigma T^{1/2}) - 1000/T$ plots for as grown T3 samples.

Although the conduction mechanisms has been easily identified for thermally evaporated samples it was impossible to select the best fitting mechanism for the e-beam evaporated samples whose conductivity decreases down to $10^{-8} (\Omega\text{-cm})^{-1}$ at low temperatures. Boron implantation has increased the conductivity of those samples and made the analysis possible. Obtained results for those samples were similar to

the thermally evaporated ones. These results have been interpreted in terms of the thermionic emission, tunneling and hopping theories as discussed in section 2.3 we investigate each of the three temperature regions over which at least one of the above conduction mechanism predominates. We found that thermionic emission over the barriers is the main conduction mechanism above 250 K. For conductive samples in the mid temperature regions 170-240 K the contribution from tunneling must also be taken into account. Hopping conduction appears to be the appropriate model to explain the temperature dependent conductivity below 160 K for all samples. In polycrystalline materials at low temperatures the carriers can not be transferred into the grain by thermionic emission, they do not have the enough energy to cross the grain barrier potential and the conduction involves the grain boundaries. In the grain boundary trapping model, the trapping states are created by the disordered atoms and the incomplete bonding among them, are distributed in the band gap. Depending on the temperature and also on the distribution of those states in the gap some of the trapping states are filled with carriers and are charged. The empty state may capture an electron from the charged states under favorable energy conditions. Then, a possibility for the conduction is by hopping of charge carriers from filled trap sates to empty trap states. The filled states may subsequently release the electron and thus help in conduction by means of hopping and photo assisted tunneling. Since filling up the trap states also rises up the Fermi level that results in lowing of the grain boundary potential and increases the probability of tunneling of the carriers.

4.4.2 Determination of Carrier Concentration and Mobility

The temperature dependent Hall-effect measurements were carried out only on the samples whose conductivity is high enough to take reliable data. All of the Hall effect measurements has been taken under the constant magnetic field strength of 970 mT. The sign of Hall-voltage showed that all the samples are *n*-type. The electron concentrations (*n*) in the CdSe thin films were calculated using the expression;

$$\frac{tV_H}{IB} = R_H = \frac{r}{ne} \quad (4.4.5)$$

where V_H is the Hall voltage, t is the film thickness and r is the Hall factor which is assumed to be equal to 1 for this study. Reliable Hall effect measurements could have been performed only on T1, T2 and boron implanted T2, E3 type samples. $\ln(\mu T^{1/2}) - 1000/T$ plots of as grown and annealed; boron implanted T2 samples is given in Fig. 4.16

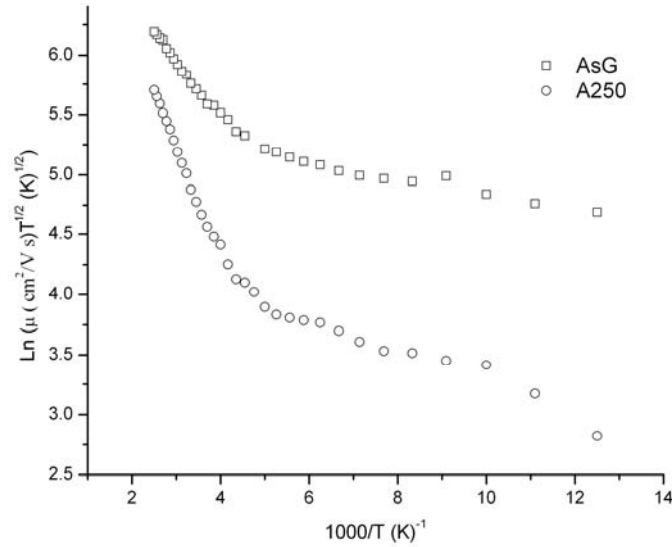


Figure 4-16: The variation of $\ln(\mu T^{1/2})$ as a function of the inverse absolute temperature for B-implanted T2 samples.

The analysis of the temperature dependent mobility were performed according to the conduction mechanism of thermionic emission where the effective mobility as a function of potential barrier height at the grain boundary, ϕ_b , is defined as

$$\mu = \mu_0 T^{-1/2} \exp\left(\frac{-q\phi_b}{kT}\right) \quad (4.4.6)$$

The slopes of $\ln(\mu T^{1/2}) - 1000/T$ plots give the barrier height, ϕ_b . For the unimplanted as-grown T2 samples barrier height is calculated to be 45.3 meV at high

temperature region (in 280-400 K). For the boron implanted samples the barrier height was found to be 44.8 meV. These results indicate that boron implantation had no effect on barrier heights before annealing. Calculated barrier heights for the unimplanted and B-implanted samples have increased to 78.4 and 83.6 meV after they have been annealed at 250 K for 30 minutes. The increase in the potential barrier can be explained with the increase in the number of trap states arising from the incomplete bondings between trap states at the grain boundary. These could be related with segregation of Se atoms which increases with annealing as observed from the EDAX results.

4.5 Photoconductivity Analysis

The temperature dependent photoconductivity measurements have been performed in the temperature range of 80-400 K at different electric field strengths and illumination intensities. In addition to dark current, the currents under the illumination of halogen lamp at light intensities 17, 34, 55, 81 and 113 mW/cm² have been measured. Also the spectral responses of the films under monochromatic light have been examined in the wavelength region of 400-960 nm.

Photoconductivity measurements were useful tools especially for the characterization of highly resistive samples. The conductivity values of e-beam evaporated samples (E1, E2, E3) increased up to 250 times at low temperature regions where the number of thermally activated carriers were very limited. Photo-current was still very significant for thermally evaporated samples (T1, T2, T3) with an increase up to 40 times at lowest temperatures. Figures 4.17a and b. give the typical current versus inverse temperature plots for thermally evaporated (T4) and e-beam evaporated (E1) samples.

Conductivity versus temperature dependencies of samples showed similar characteristics under illumination and in dark. The only expectation occurred for the boron implanted T2 samples. Conductivity of this sample decreased under illumination with increasing temperature while the dark conductivity increased in the same way with the other samples. Since most of the carriers have been excited to conduction band optically, activation energies calculated from the slope of $\ln(\sigma T^{1/2}) - 1000/T$ plots has decreased with increasing illumination power.

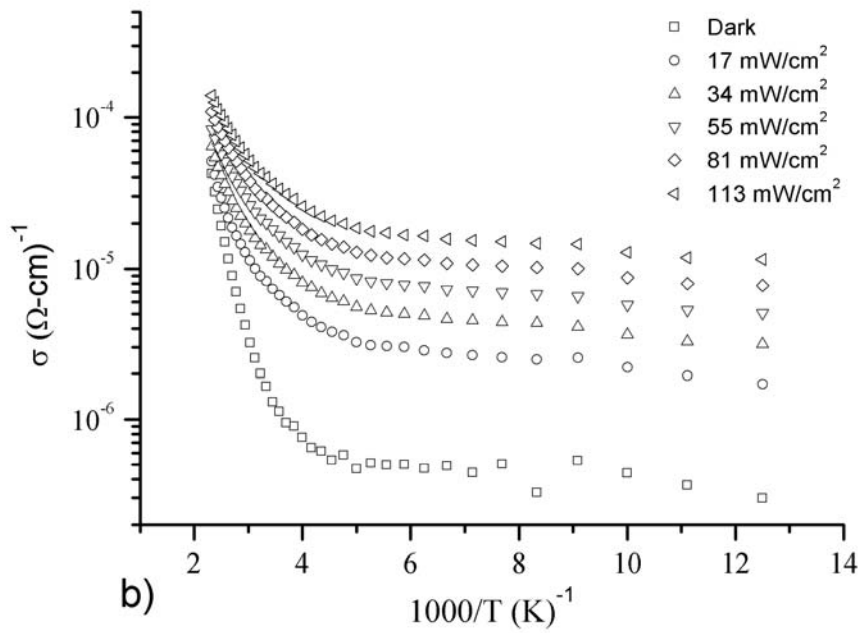
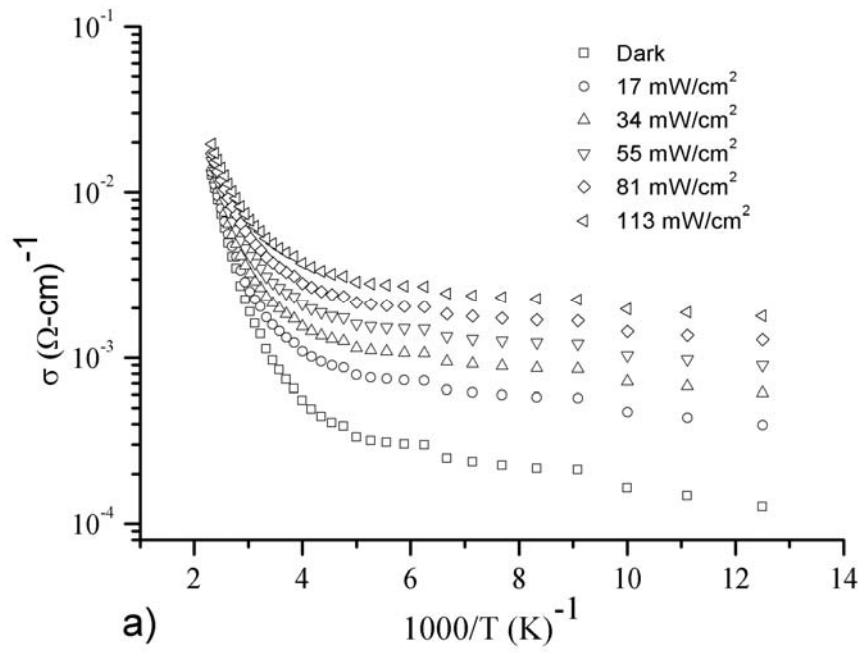
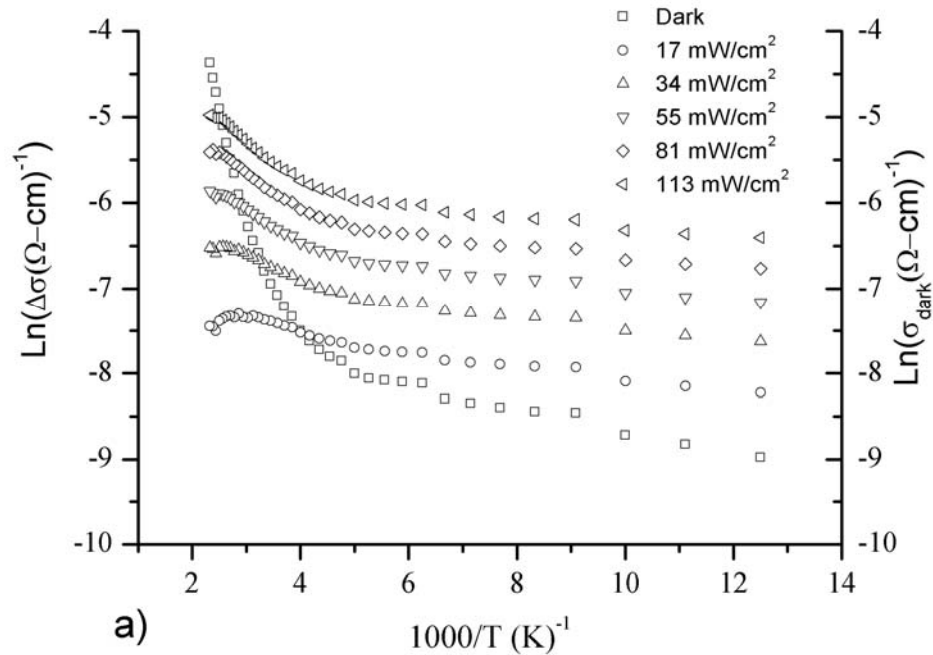


Figure 4-17: Variation of conductivity as a function of inverse absolute temperature for as grown a) T2 and b) E1 samples.

The photoconductivity has been calculated by subtracting the dark conductivity from the measured conductivity under illumination. The photoconductivity increases with the increasing temperature until the number thermally activated carriers exceeds the number of optically excited ones. Since the recombination limits the number of carriers in the conduction band after this critical temperature photoconductivity starts to decrease. This phenomena is called thermal quenching as discussed in section 2.4.3. The value of the critical temperature depends on the photo-excitation intensity, i.e. increases with the increasing intensity. Intersection of dark conductivity with the critical temperature points is more clearly visible for the e- beam evaporated samples which are more sensitive to light. Critical temperatures are slightly larger than the temperatures at which dark current equals to photocurrent for thermally evaporated ones. But the correlation is still visible. Dark current and photo current versus inverse temperature plots of as grown T2 and E1 samples are given in Fig 4.18 a and b.



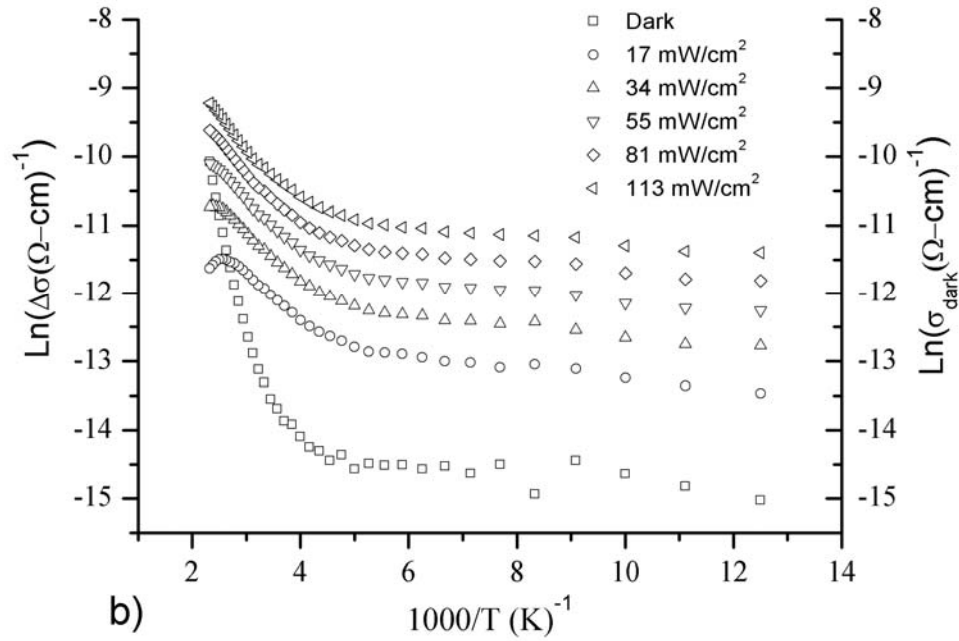


Figure 4-18: The variation of photoconductivity as a function of inverse temperature at different illumination intensities for as grown a) T2 and b) E1 samples.

Characteristic of the recombination centers has been determined from the photocurrent versus illumination intensity plots at different temperatures and applied fields. Fig. 4.19 and Fig.4.20 gives the $\ln I_{ph}$ versus $\ln \phi$ plots of as-grown T2 and E1 samples at different temperatures and applied electric fields, respectively. Linear characteristics have been observed at each temperature for both samples. Results indicate that photocurrent depends on illumination intensity as $I_{ph} \propto \phi^n$. n values have been calculated to be in the range of 0.92 -1.26 and 0.93-1.12 for the two reference samples mentioned above. Observed sublinear and supralinear photoconductivity regions can be explained with the two center recombination model discussed in section 2.4. n values are greater than 1 in high temperature region and in lowest temperature region (for e- beam evaporated samples only) indicating the existence of two donor levels dominant at low and high regions of the examined temperature range.

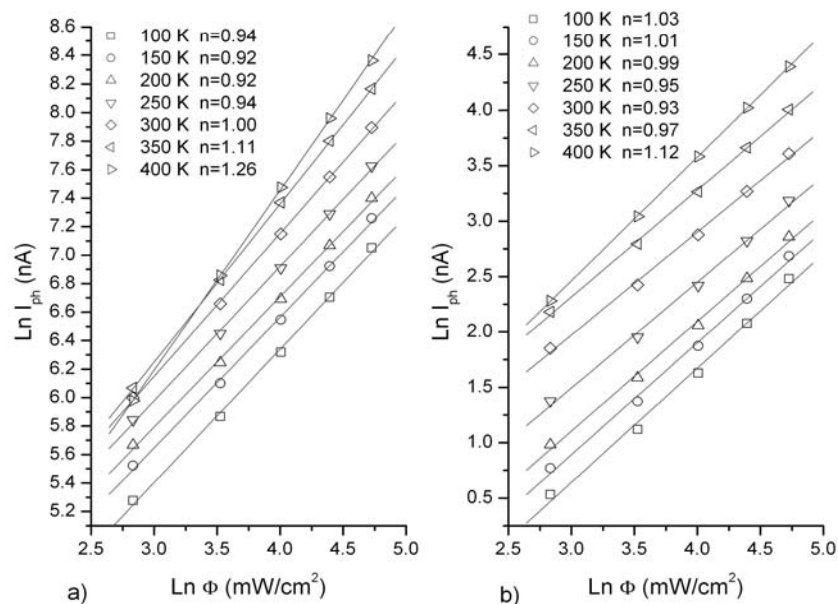


Figure 4-19: Photocurrent-illumination intensity behavior at different temperatures for as-grown a) T2 and b) E1 samples.

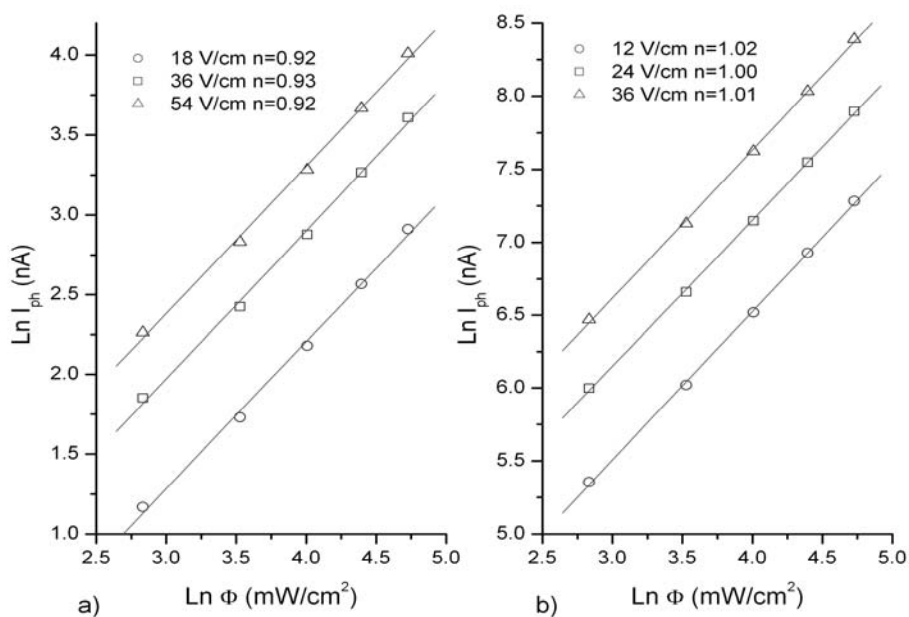


Figure 4-20: Photocurrent-illumination intensity behavior at different applied electric fields for as grown a) T2 and b) E1 samples.

In addition to illumination dependent photoconductivity measurements wavelength dependent photoconductivity measurements have been performed. For these measurements a 150 Watt halogen lamp and a monochromator has been used. Measurements have been performed in the temperature range of 100 and 375 K. Photocurrent has been calculated by subtracting the dark current from the measured current under illumination. Finally, photocurrent values have been normalized using the illumination spectrum of the light given in the Fig. 3.11. Fig. 4.21 a, b and c gives the photo current values as a function of photon energy for as-grown T2 and boron implanted T2 and E3 samples respectively.

Photocurrent versus $h\nu$ plots show that the maximum value of the photocurrent for as grown and un-implanted samples is around 1.72 eV. This value is the same with the optical band gap calculated from the transmission measurements for this sample, indicating that same energy level in the energy band is responsible for optical absorption and photocurrent. After this point photocurrent decreases very slightly in 1.72- 1.85 eV region.

On the other hand for the boron implanted samples the optical behavior is a little bit different. For both thermally evaporated T2 and e-beam evaporated E3 samples the photocurrent reaches to a maximum value at 1.85 eV and start to decrease immediately after this point. This could be the effect of deep trap levels introduced by the implantation and disorder in the structure of films.

In parallel with the conductivity and illumination dependent photoconductivity results photoconductivity of the samples increases slightly when they are annealed at 250° C but decreased below the as-grown value with further annealing at 300 K. The photon energy causing the maximum photocurrent has not changed with annealing as shown in Fig. 4.22.

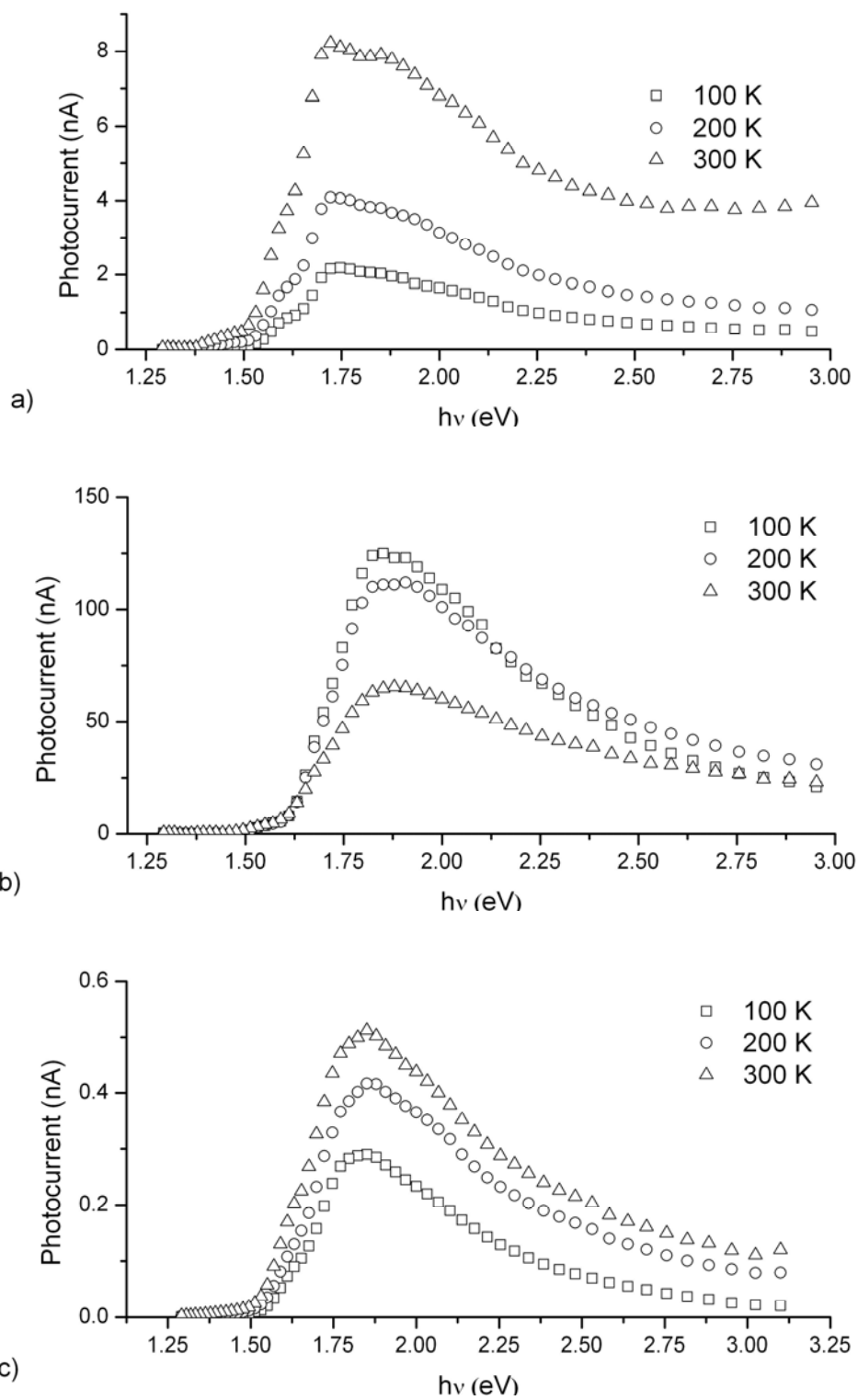


Figure 4-21: Photocurrent as a function of incident photon energy at different temperatures for as grown a) T2, b) B-imp T2 and c) B-imp E3 CdSe thin films.

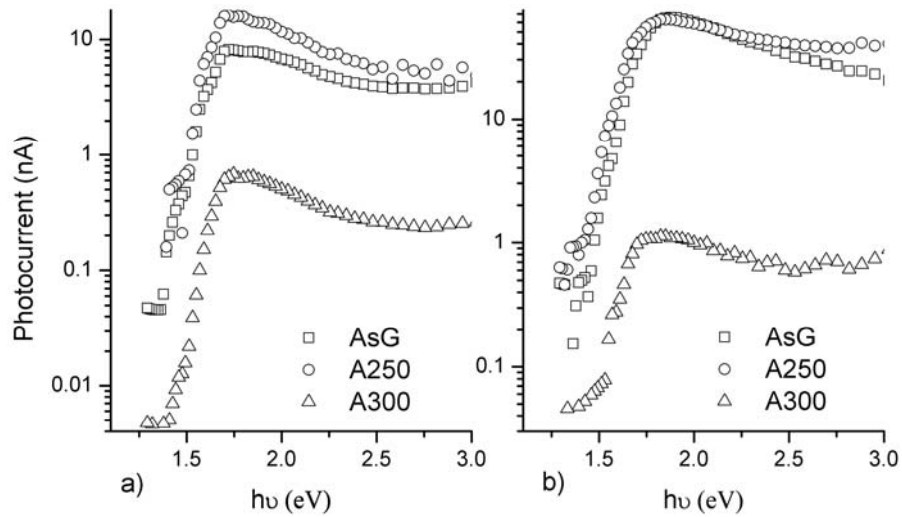


Figure 4-22: Photocurrent as a function of incident photon energy at 300°K for a) T2, b) B-imp T2 CdSe thin film after various annealing steps.

Another important observation was the decrease in the photoconductivity with the increasing temperature for B implanted T2 samples. The same temperature dependence has also been observed in the wavelength dependent photocurrent measurements of the sample. On the other hand e-beam evaporated, B-implanted samples behaved like unimplanted ones as seen in Fig. 4.12.c. Plots of illumination dependent and wavelength dependent photocurrent are given in Fig. 4.13 and 4.12b respectively. The negative temperature dependence of photocurrent has been disappeared after the sample is annealed at 250°C. After they have been annealed at 250 and 300°C, the results obtained for the un-implanted and B-implanted samples gave similar values. It shows that these behaviors could be related with increasing disorder in the grain and/or in the grain boundary regions for polycrystalline materials because effect of annealing and/or activating the implanted boron atoms.

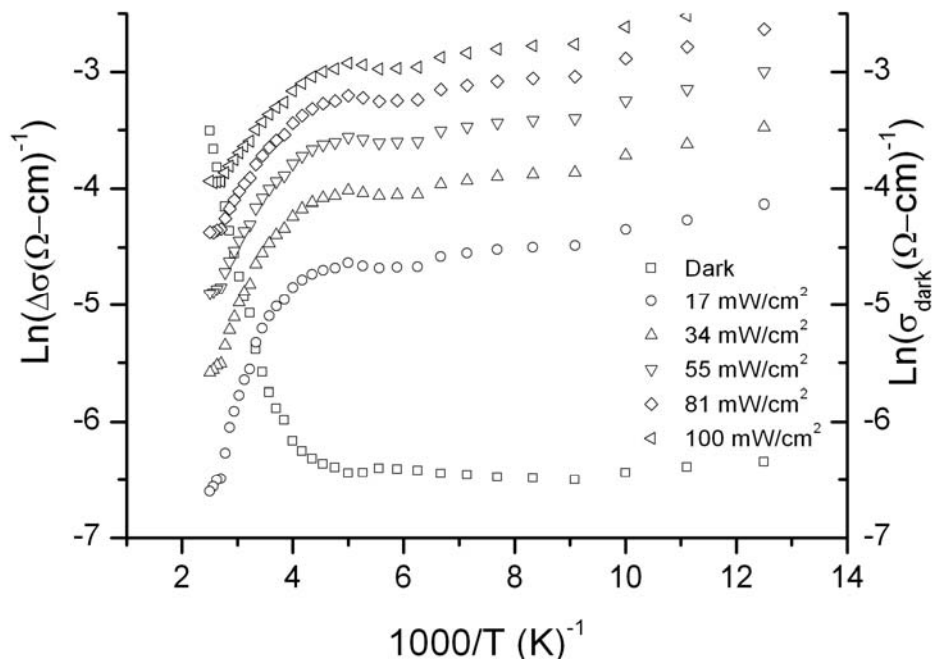


Figure 4-23: The variation of photoconductivity as a function of inverse temperature at different light intensities for as grown boron imp(T2) samples.

CHAPTER 5

CONCLUSIONS

The aim of this study was to investigate and compare structural, optical and electrical properties of the CdSe thin films deposited by thermal evaporation and e-beam evaporation techniques and to investigate the effects of low dose boron implantation on these properties.

The compositional analysis performed with EDAX indicated that almost stoichiometric CdSe thin films with excess cadmium smaller than 1% are deposited with both of the deposition methods. A systematic decrease in the Se content has been observed in the EDAX patterns as the annealing temperature increases. Same patterns also showed that annealing of the films under rough vacuum conditions does not enhance Se evaporation but prevents the contamination of the films. In parallel with the EDAX results, identification of the peaks in the XRD patterns has confirmed that only the hexagonal and cubic phases of the CdSe exists in the films. Elemental Cd or Se peaks did not appear in XRD patterns. It has been observed that all of the films were highly oriented in (002_h) planes parallel to the substrate. Grain sizes of the films have been calculated using Scherrer formula and found to be varying between 40 - 95 nm. Almost no significant changes have been occurred in the XRD patterns as a result of annealing. The associated changes in the crystallinity and grain size were only marginal.

The results of optical analysis showed that optical absorption in the CdSe thin films takes place through allowed direct interband transition. Variation $(\alpha h\nu)^2$ as a function of $h\nu$ has been plotted for all samples to determine the band gap energy. Two linear regions have been observed in plots indicating the existence of two different band gap energy values, which may be attributed to the spin orbit splitting of the valance band. The low values of the energy band gap varied between 1.64 and 1.68 eV while the high values which have been obtained from the extrapolation of

the second linear region found to be varying between 1.66 and 1.91 eV. Annealing of the samples even at the high temperatures up to 500°C, have not created any observable changes in the optical band gap energy. These results support the XRD measurements which indicate that crystallinity and grain sizes of the samples do not change during annealing. Low dose (1×10^{15} ions/cm²) boron implantation did not create any observable sign in the optical and structural results of thermally evaporated and e-beam evaporated CdSe thin films.

The distinct behaviors between thermally evaporated and e-beam evaporated CdSe thin films were observed during the investigation of electrical properties. Room temperature conductivity values of thermally evaporated as-grown films varied between 9.4 and 7.5×10^{-4} ($\Omega\text{-cm}$)⁻¹. It has been observed that conductivity of the films decreases with the increasing substrate temperature. The decrease in the conductivity can be explained with the decrease in the point defects and consequent decrease in the number of free electrons in the conduction band with the increasing substrate temperature. On the other hand, significantly higher resistivity values have been measured for e-beam evaporated samples. Room temperature conductivity values of as-grown samples produced with this method varied between 1.6×10^{-6} and 5.7×10^{-7} ($\Omega\text{-cm}$)⁻¹. Similar decreasing behavior in conductivity with increasing substrate temperature has been observed in e-beam evaporated CdSe thin films. In addition to deposition method, boron implantation has resulted significant changes in electrical conductivity of the samples. Room temperature conductivity values of the as grown samples have increased 5 and 8 times for thermally evaporated and e-beam evaporated samples respectively. Post annealing at 250°C has increased the conductivity of the unimplanted and B implanted samples slightly but the conductivity has drop below the as grown value when the samples annealed at 300°C. This implies that boron atoms in structure are activated with annealing and result in disordered structure in the grain boundary regions.

The Hall mobility measurements could only be performed for the samples which are conductive enough to give reliable data. The Hall effect measurements have showed that the films are *n*-type. This result has been expected since the films are known to be Cd rich from the EDAX results. The mobility values were found to vary in between 8.8 and 86.8 cm²/V-s depending on the annealing temperature and

film thickness. The temperature dependence of the mobility showed an exponential behavior at high temperature region (250-400 K). Calculated grain boundary barrier height was found to be in the order of kT allowing the thermionic emission model to apply to the transport properties of the samples.

Photoconductivity measurements have revealed that e-beam evaporated samples have better photo-response as a result of to their higher dark resistivity. Photoconductivity results also indicated that photocurrent depends to illumination intensity as $I_{ph} \propto \phi^n$. n values have been calculated to be between 0.92 -1.26 and 0.93-1.12 at various temperatures for thermally evaporated and e-beam evaporated samples, respectively. For those samples n values has decreased until a 200 and 300 K, respectively and then started the increase. The variation of n indicates the existence of supralinear-sublinear-sublinear regions respectively with increasing temperature. These results may be explained with the existence of two discrete set of donor levels dominating at different temperature ranges one is at the low edge the other is at the high edge of temperature range of measurements. Illumination wavelength versus photocurrent measurements indicated that maximum photo current passes through the unimplanted samples when the incident photons have energy of 1.72 eV which equals to the optical energy band gap calculated for these samples. For both of the e-beam and thermal evaporated samples the maximum photocurrent has been observed at 1.85 eV after B implantation.

In general the electrical properties of the CdSe thin films are strongly affected by the deposition conditions such as deposition method, substrate temperature, B implantation. and post depositional annealing while the structural and optical properties are less sensitive to them. These results indicate that deposition conditions do not affect the grains as much as it does the grain boundaries.

Thermal evaporation and e-beam evaporation offers many possibilities to modify the deposition parameters and to obtain films with determined resistivities without changing the compositional, structural and optical properties. Implantation with suitable elements is also a good method to tailor the thin film properties. Boron implantation has given well results since it has significantly enhanced electrical parameter without changing the structural and optical properties.

For further study, we will try to make a detailed analysis of transient photo-response of CdSe thin films in order to investigate the electronic density of the trap states as well as the recombination processes. We will also carry out space charge limited conduction measurements to determine the trap levels and trap behaviors.

REFERENCES

- [1] G. Moersch, P. Rava, F. Schwarz, A. Paccagnella, *IEEE Trans, Electron Devices*, ED-36, (1989), 449.
- [2] A. Van Calster, F. Vanfletern, I. De Rycke, J. De Baets, *J. Appl. Phys.*, 64, (1998), 3282.
- [3] T. Gruszecki and B. Holmstrom, *Sol. Energy Mater. Sol. Cells*, 31, (1993), 227.
- [4] A.K. Pal, A. Mondal and S. Chaudhuri, *Vacuum*, 41, (1990), 1460.
- [5] K. Shimizu, O. Yoshida, S. Aihara and Y. Kiuchi, *IEEE Trans. Electron Devices*, ED-18, (1971), 1058.
- [6] V.A. Smyntyna, V. Gerasutenko, S. Kashulis, G. Mattongo and S. Reghini, *Sensors Actuators B*, 19, (1994), 464.
- [7] N.G. Patel, C.J. Panchal and K.K. Makhijia, *Cryst. Res. Technol.*, 29, (1994), 1013.
- [8] B. Bonello and B. Fernandez, *J. Phys. Chem. Solids*, 54, (1993), 209.
- [9] B.J. Curtis, H. Kiess, H.R. Brunner and K. Frick, *Photogr. Sci. Eng.*, 24 (1980), 244.
- [10] O. Oduor and R.D. Gould, *Thin Solid Films*, 317, (1998), 409.
- [11] K.P. Mohanchandra and J. Uchil, *Thin Solid Films*, 305, (1997), 124.
- [12] M.J. Lee and Shis-Chung Lee, *Solid State Electr.*, 43, (1999), 833.
- [13] D. Samanta, B. Samanta, A.K. Chaudhuri, S. Ghorai and U. Pal., *Semicond. Sci. Technol.*, 11, (1996), 548.
- [14] U. Pal, D. Samata, S. Ghorai and A.K. Chaudhuri, *J. Appl. Phys.*, 74 (1993), 6368.
- [15] C.M. Rouleau and D.H. Lowndes, *Appl. Surf. Sci.*, 127–129, (1998), 418.
- [16] M. Ohishi, M. Yoneta, H. Saito, H. Sawanda and S. Mori, *J. Cryst. Growth*, 184/185, (1998), 57.

- [17] H. Cachet, R. Cortes, M. Froment and A. Etcheberry, *Thin Solid Films* 361–362, (2000), 84.
- [18] M.A. Russak and J. Reichman, *J. Electrochem. Soc.*, 129, (1982), 542.
- [19] F. Shizuo, Wu Yi-hong, K. Yoichi and F. Shigeo, *J. Appl. Phys.*, 72, (1992), 5233.
- [20] G. Perna, V. Capozzi, S. Pagliara, M. Ambrico and D. Lojacono, *Thin Solid Films*, 387, (2001), 208.
- [21] S.J. Lade, M.D. Uplane and C.D. Lokhand, *Mater. Chem. Phys.*, 68, (2001), 36.
- [22] V. Swaminathan and K.R. Murali, *Sol. Energy Mater. Sol. Cells*, 63, (2000), 207.
- [23] S.S. Kale and C.D. Lokhande, *Mater. Chem. Phys.*, 62 (2000), 103.
- [24] K. Singh and S.S.D. Mishra, *Sol. Energy Mater. Sol. Cells*, 63, (2000), 275.
- [25] C. Baban, G. I. Rusu, *Appl Surf. Sci.*, 221, (2003), 6.
- [26] E. Parthe, “*Crystal Chemistry of Tetrahedral Structures*”, Gordon and Breach, New York, 1964.
- [27] S. S. Devlin, in “*Physics and Chemistry of II-VI Compounds*”, edited by M. Aven and J. S. Prener, North-Holland, Amsterdam, 1967.
- [28] K. J. Siemsen and H. D. Riccius, *Phys. Status Solidi*, 37, (1970), 445.
- [29] S. Velumani et al., *Sol. Ener. Mat. And Sol. Cells*, 76, (2003), 347.
- [30] S. Velumani, Sa K. Narayandass and D. Mangalaraj, *Semicond. Sci. Technol.*, 13, (1998), 1016.
- [31] S. Kr. Sharma et al., *Optical Materials*, 13, (1999), 261.
- [32] Sathyalatha K C, Uthanna S and Jayaramareddy P., *Thin Solid Films*, 174, (1989), 233.
- [33] Pawlikowski J M., *Thin Solid Films*, 190, (1990), 39.
- [34] Pradip KR. Kalita, B. K. Sarma and H. L. Das, *Bull. Mater. Sci.*, 26, No. 6, (2003), 613.
- [35] Nesheva D., *Thin Solid Films*, 280, (1996), 51.
- [36] Raoult F, Fortin B and Colin Y., *Thin Solid Films*, 182, (1989), 114.
- [37] V. A. Fedorov, V. A. Gaushin, and Yu N. Korkishko, *Phys. Status Solidi A*, 126, K5 (1991)

- [38] Chin-Yu Yeh, Z. W. Lu, S. Froyen, and Alex Zunger, Phys. Rev.B, 45 (12), (1992), 130.
- [39] A. G. Lehmann, M. Bionducci and F. Buffa, Phys. Rev. B, 58, (1998), 5275.
- [40] wikipedia.org/wiki/Cadmium_selenide.
- [41] R. Tenne et al., Phys. Rev. B, 42(3), (1990), 1763.
- [42] T. Çolakoğlu “*The Growth and Characterization of GaSe Thin Films* ”, Ms. Thesis, METU, (2003).
- [43] A. Elshabini-Riad and F. D. Barlow, “*Thin Film Technology Handbook*” McGraw Hill, (1998).
- [44] J. Volger, Phys Rev., 9, (1950), 1023.
- [45] R. L. Petritz, Phys Rev., 104, (1956), 1508.
- [46] H. Berger, Phys Status Solidi, 1, (1961), 739.
- [47] H. Berger, W. Kahle and G. Janiche, Phys Status Solidi, 28, (1968), 97.
- [48] J. Y. W. Seto, J. Electrochem Soc., 122, (1975), 701.
- [49] J. Y. W. Seto, J. Appl Phys, 46 (1975), 5247.
- [50] R. G. Mankarious, Solid-State Electron., 7, (1964), 702.
- [51] M. V. Garcia-Cuence, J. L. Morenza and J. Esteve, J. Appl. Phys., 56, (1984), 1738.
- [52] J. G. Simmons, J. Appl. Phys., 34, (1963), 1793.
- [53] P.W. Anderson, Phys. Rev., 109, (1958), 1492.
- [54] N.F. Mott and E. A. Davis, “*Electronic Processes in Non-Crystalline Materials*”, Clarendon Press, Oxford (1971).
- [55] N. F. Mott, J. Non-Cryst. Solids, 1, (1968), 1.
- [56] R. H. Bube, “*Electrons in Solids: An Introductory Survey*” San Diego, Academic Press, (1992).
- [57] R. H. Bube, “*Photoelectronic Properties of Semiconductors* ”, Cambridge University Press, (1992).
- [58] L. L. Kazmerski, “*Polycrystalline and Amorphous Thin Film and Devices* ” Academic Press, New York, (1980).
- [59] M. Parlak, “*Characterization of InSe Thin Films*”, Ph.D Thesis, METU, (1996).

- [60] J. Yeager and M. A. Hrusch-Tupha, “*Low level measurements*”, Ohio, Keithley Instruments. Inc. (1998).
- [61] R. B. Kale and C.D. Lokhande, *Semicon. Sci. Technol.*, 20, (2005), 1.
- [62] C. Baban, G.I.Rusu, *Appl. Surf. Sci.*, 6, (2003), 12.
- [63] J. C. Erskine and A. Cserhati, *J. Vac. Sci. Technol.*, 15(6), (1978), 1823.
- [64] B.D. Cullity, “*Elements of X-ray Diffraction*” Addison-Wesley, MA, 1972.
- [65] F.R. Shepherd et al, *J. Vac. Sci. Technol.*, 18(3), (1981), 899.
- [66] R. Swanepoel, *J. Phys. E: Sci. Instrum.*, 16, (1983), 1214.
- [67] U. Pal, D. Samanta, S. Ghorai, A. K. Chaudhuri, *J. Appl. Phys.*, 74, (1993), 6368.
- [68] G. M. K. Thutupalli and S. G. Tomlin, *J. Phys. D*, 9, (1976), 1639.
- [69] A. Mondal et.al, *J. Matter. Sci.*, 25, (1990), 2221.
- [70] C. R. Tellier, *Thin Solid Films*, 51, (1978), 371.
- [71] K. P. Mohanchandra and J. Uchil, *J. Appl. Phys.*, 84, (1998), 306.